Current-driven domain wall motion in ferrimagnetic nanowires

K. Y. Jing [1,2] Zhou-Zhou Sun, [1,2,3] and X. R. Wang [1,2,4,*]

[1] *Physics Department, The Hong Kong University of Science and Technology, Clear Water Bay, Kowloon, Hong Kong*
[2] *HKUST Shenzhen Research Institute, Shenzhen 518057, China*
[3] *School of Computer, South China Business College, Guangdong University of Foreign Studies, Guangzhou 510545, China*
[4] *William Mong Institute of Nano Science and Technology, The Hong Kong University of Science and Technology, Clear Water Bay, Kowloon, Hong Kong, China*

(Received 5 January 2024; revised 14 May 2024; accepted 25 July 2024; published 7 August 2024)

Current-driven DW motion in a ferrimagnetic (FiM) nanowire through spin transfer torques (STTs) is explained by the energy-work principle. An adiabatic STT (a-STT) can be incorporated into the Lagrangian as an energy functional and tends to twist DW planes. DWs in homogeneous FiM nanowires can resist an a-STT from moving below a critical value proportional to the maximal transverse anisotropic field. Second, a nonadiabatic STT (na-STT) cannot be included in the Lagrangian and can enter the spin dynamics through the Rayleigh functional. A static DW cannot exist under a na-STT such that a DW in a homogeneous FiM nanowire must propagate under an arbitrarily small na-STT. Third, STTs do positive work on a DW which must compensate by energy dissipated by moving spins inside the DW through damping. Below the Walker breakdown current, the na-STT does positive work and the a-STT does no work. Above the Walker breakdown, a DW starts to precess around the wire axis during its propagation along the axis. Whether the a-STT does a negative or a positive work depends on the direction of the DW precession, while the na-STT still does a positive work. Last, a DW velocity formula is obtained, which agrees with simulations both below and above the Walker breakdown current. In the vicinity of the angular momentum compensation point, the precession frequency of a DW reaches its maximum, and the DW structure is distorted. The DW distortion and spin wave emission modify the DW motion, which deviates from its linear dependence on current density. This theory explains well the observed DW mobility near the angular momentum compensation point of FiM nanowires and resolves the puzzle of the unphysical negative na-STT problem.

DOI: 10.1103/PhysRevB.110.054414

I. INTRODUCTION

Magnetic domain walls (DWs) are solitons [1–3] which are topologically protected from annihilation and creation in the bulk of a material because a transformation from a DW to a different state such as a topologically trivial single domain needs to overcome an infinite potential barrier. DWs can be easily manipulated by many external stimuli such as magnetic fields [4], electric currents [5–10], spin waves [11,12], and thermal gradient [13]. The fundamental interest [14,15] and promising applications [16] of DW dynamics have attracted much attention in recent years, especially for the current-driven DW-motion.

One goal in DW research is to achieve stable high DW velocity at least hundreds of meters per second. The hurdle of achieving this goal in ferromagnets is the low Walker breakdown fields/currents beyond which DW mobility drops significantly. One recent breakthrough is high DW velocity of over 1000 meters per second and high Walker breakdown fields/currents observed in ferrimagnetic (FiM) nanowires near the so-called angular momentum compensation point (AMCP) [17–40].

Tunability of ferrimagnets are much higher than their ferromagnetic counterparts. A ferrimagnet has at least two spin sublattices antiferromagnetically coupled with each other and may have an AMCP, at which the angular momenta of the two sublattices cancel each other, and a magnetization compensation point, at which the magnetizations cancel each other. Magnetization and angular momentum are not the same, but related. Magnetization interacts with a magnetic field while the angular momentum moves under a torque as described by the Landau-Lifshitz-Gilbert (LLG) equation. They do not need to appear and disappear together although they do in many ferrimagnets. Rare-earth-transition-metal (RE-TM) alloys are one class of ferrimagnets whose AMCP and magnetization compensation point are generally different and can be tuned by temperature and by the compositions [19,41].

An electric current interacts with DWs in magnetic nanowires through two spin-transfer torques (STTs) [5,6,42]: an adiabatic STT (a-STT) and a nonadiabatic STT (na-STT). Different from a static magnetic field that can create an energy density difference between two domains separated by a DW, STTs do not change the energy density of homogeneous domains. Field-driven DW motion is caused by energy density differences between two domains, and DW speed is proportional to the energy dissipation [4,40,43,44]. However,

*Contact author: phxwan@ust.hk

current-driven DW motion is generally believed to be caused by an angular momentum transfer, even though a DW does not always propagate along the direction of electron movement in multilayer wires [45]. Despite all the fundamental differences in DW driving mechanisms, one puzzle is the great similarities between field-driven and current-driven DW motion. For example, both exhibit Walker breakdown phenomenon [4] below which DWs undergo a rigid-body motion and above which an oscillatory DW motion appears [6,9,46–48]. The unified approach in the field is the collective mode theory that assumes DWs as rigid-bodies and can be described by their centers and DW plane angles [20,29–35].

Although collective mode theory brought us many good understandings of DW motion under various driven forces such as the linear responses to the field/current below the Walker breakdown field/current, existing theories [20,29–35] encounter difficulties in understanding the experimentally [20] and numerically [29,34] observed DW motion at high field/current and, especially, around the AMCP when the rigid-body assumption is violated [34]. Recently, it was shown that both high and low field-driven DW motion can be understood from the energy balance viewpoint at both qualitative level and highly quantitative level [40,43,44]. Naturally, one may ask whether the energy balance can be used to understand current-driven DW motion and overcome the difficulties of collective mode theory in explaining high current DW motion and nonlinear DW dependence on the current near the AMCP, as well as the negative na-STT problem [20].

In this paper, we present a theory of current-driven DW motion based on the generic FiM dynamics [49,50] and the energy-work principle. We show that in a homogeneous FiM nanowire, static DWs can exist under a small a-STT while DWs must move under an arbitrarily small na-STT. During the DW motion, STTs do an overall positive work which compensates the dissipated energy of moving spins inside DW. Based on the energy-work principle, a DW velocity formula, applicable both below and above the Walker breakdown current, was obtained. This theory explains the experimentally observed current-driven DW motion and resolves the negative na-STT puzzle [20].

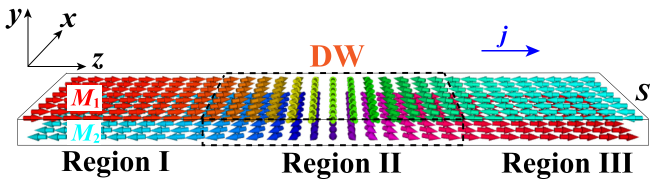

FIG. 1. Schematic diagram of a head-to-head DW in a FiM nanowire. Region I and III are two uniform FiM domains, separated by a DW (region II) whose width is Δ. $\boldsymbol{j}$ is the electric current density. Colors denote the spin orientations: red for spins along $+\hat{z}$ and light blue for spins along $-\hat{z}$. S is the cross-section area of the wire.

II. MODEL AND METHODOLOGY

A. Domain walls in FiM wires

Figure 1 schematically illustrates a FiM strip consisting of two antiferromagnetically (AFM) coupled ferromagnetic layers (sublattices) labeled by $\ell(=1,2)$, called A-type ferrimagnet. It is believed that general DW features of A-type ferrimagnet should be applicable to all types of ferrimagnets. The easy-axis is along the wire axis defined as the z axis. A head-to-head (HH) DW is at the center of the wire and an applied uniform current of density j is along the z axis. $\boldsymbol{M}_\ell = M_\ell \boldsymbol{m}_\ell$ are the magnetization of the two sublattices with M_ℓ and $\boldsymbol{m}_\ell$ being the saturation magnetization and unit vector of the magnetization. In terms of polar and azimuthal angles θ_ℓ and ϕ_ℓ, the three Cartesian components are $\boldsymbol{m}_\ell = (\sin\theta_\ell\cos\phi_\ell, \sin\theta_\ell\sin\phi_\ell, \cos\theta_\ell)$. The Lagrangian density functional describing the nanowire is $\mathcal{L} = \mathcal{T} - \varepsilon$, consisting of kinetic energy density functional $\mathcal{T} = -\sum_{\ell=1,2} s_\ell \cos\theta_\ell \partial_t\phi_\ell$ and potential energy density functional $\varepsilon = \varepsilon_{\rm m} + \varepsilon_{\rm a}$ [49,50]. $\varepsilon_{\rm m} = J\boldsymbol{m}_1\cdot\boldsymbol{m}_2 + \sum_{\ell=1,2}[A_\ell(\nabla\boldsymbol{m}_\ell)^2 + f_\ell(\boldsymbol{m}_\ell)]$ is the magnetic energy functional, $\varepsilon_{\rm a}$ (discussed below) is the energy density functional from the a-STT. $s_\ell = M_\ell/\gamma_\ell$ and $\gamma_\ell = g_\ell\mu_B/\hbar$ are the spin densities and gyromagnetic ratios of sublattice ℓ, and g_ℓ, μ_B, and $\hbar$ are, respectively, the Landé g-factor of ℓth sublattice, the Bohr magneton, and the Planck constant. J is the interlayer AFM coupling constant, A_ℓ and f_ℓ are the exchange stiffness and magnetic anisotropy energy of sublattice ℓ. f_ℓ has two equal minimum at $\boldsymbol{m}_\ell = \pm\hat{z}$. Below the Greek subscripts $\mu, \nu = 0, 1, 2, 3$ denote t, z, x, y, and the Latin subscript $i = 1, 2, 3$ denote z, x, y. The Einstein summation convention for repeated subscripts of both Greek and Latin letters is applied, while this convention is not applied to the sublattice index ℓ. The Gilbert damping is described by the Rayleigh dissipation functional $R_\alpha = \int \mathcal{R}_\alpha d^3\boldsymbol{x}$, with the Rayleigh dissipation density $\mathcal{R}_\alpha = \frac{1}{2}s_1\alpha_{11}(\partial_t\boldsymbol{m}_1)^2 + \frac{1}{2}s_2\alpha_{22}(\partial_t\boldsymbol{m}_2)^2 + \frac{1}{2}(\frac{\alpha_{12}s_2\gamma_2}{\gamma_1} + \frac{\alpha_{21}s_1\gamma_1}{\gamma_2})(\partial_t\boldsymbol{m}_1\cdot\partial_t\boldsymbol{m}_2)$, α_{11}, α_{22} and α_{12}, α_{21} are intrasublattice and intersublattice damping coefficients. We have $\alpha_{12}s_2\gamma_2/\gamma_1 = \alpha_{21}s_1\gamma_1/\gamma_2$ due to the action-reaction law [49,50]. When a spin polarized electric current passes through the DW, the exerted STTs on the local spins take the form of $\boldsymbol{\tau}_\ell = \boldsymbol{\tau}_{{\rm a},\ell} + \boldsymbol{\tau}_{{\rm na},\ell}$, where $\boldsymbol{\tau}_{{\rm a},\ell} = -\frac{P_\ell\hbar}{2e}\partial_z\boldsymbol{m}_\ell$ is the a-STT and $\boldsymbol{\tau}_{{\rm na},\ell} = \frac{\beta_\ell P_\ell\hbar}{2e}\boldsymbol{m}_\ell\times\partial_z\boldsymbol{m}_\ell$ is the na-STT. $\boldsymbol{j}$, β_ℓ, P_ℓ and $e\,(>0)$ are electric current density, the nonadiabaticity coefficients, spin polarizations for ℓth sublattice and the electron charge, respectively. The a-STT can be included in the Lagrangian by adding a term of $E_{\rm a} = \sum_{\ell=1,2}\int \boldsymbol{j}\cdot\boldsymbol{\mathcal{A}}_\ell d^3\boldsymbol{x}$ [9,14], i.e., $\boldsymbol{\tau}_{{\rm a},\ell} = \boldsymbol{m}_\ell\times\frac{\delta E_{\rm a}}{\delta\boldsymbol{m}_\ell}$. $\boldsymbol{\mathcal{A}}_\ell = -\frac{P_\ell\hbar}{2e}\phi_\ell\nabla\cos\theta_\ell$ is not unique and subjects to following gauge-transformation $\boldsymbol{\mathcal{A}}_\ell \to \boldsymbol{\mathcal{A}}_\ell + \nabla\Lambda(\theta_\ell,\phi_\ell)$ for an arbitrary functional Λ of θ_ℓ, ϕ_ℓ. However, na-STT enters the dynamics through the Rayleigh functional by adding a term of $R_{\rm na} = \sum_{\ell=1,2}\int\mathcal{R}_{{\rm na},\ell}d^3\boldsymbol{x}$ with the corresponding functional density $\mathcal{R}_{{\rm na},\ell} = \frac{\beta_\ell P_\ell\hbar}{2e}(\partial_t\boldsymbol{m}_\ell)\cdot(j_i\partial_i\boldsymbol{m}_\ell)d^3\boldsymbol{x}$, i.e., Rayleigh functional $R = \int\mathcal{R}d^3\boldsymbol{x} = R_\alpha + R_{\rm na}$. Using Euler-Lagrange equations

$$\partial_\mu\left(\frac{\partial\mathcal{L}}{\partial(\partial_\mu q_\ell)}\right) - \frac{\partial\mathcal{L}}{\partial q_\ell} + \frac{\partial\mathcal{R}}{\partial(\partial_t q_\ell)} = 0, \tag{1}$$

in terms of generalized coordinates $q_\ell = \theta_\ell, \phi_\ell\ (\ell = 1, 2)$, the FiM magnetization dynamics in the presence of STTs is governed by [49,50]

$$s_1\partial_t \boldsymbol{m}_1 = -\boldsymbol{m}_1 \times \left(-\frac{\delta E_\mathrm{m}}{\delta \boldsymbol{m}_1} - \alpha_{11}s_1\partial_t\boldsymbol{m}_1 - \frac{\alpha_{12}s_2\gamma_2}{\gamma_1}\partial_t\boldsymbol{m}_2\right) + \boldsymbol{\tau}_1,$$
$$s_2\partial_t \boldsymbol{m}_2 = -\boldsymbol{m}_2 \times \left(-\frac{\delta E_\mathrm{m}}{\delta \boldsymbol{m}_2} - \alpha_{22}s_2\partial_t\boldsymbol{m}_2 - \frac{\alpha_{21}s_1\gamma_1}{\gamma_2}\partial_t\boldsymbol{m}_1\right) + \boldsymbol{\tau}_2, \qquad (2)$$

where $-\mu_0^{-1}\delta E_\mathrm{m}/\delta \boldsymbol{M}_\ell \equiv \boldsymbol{H}_\ell$ are effective fields on $\boldsymbol{M}_\ell$, and μ_0 is the vacuum permeability.

It is interesting to notice the opposite results of STTs in homogeneous magnetic states. There, Slonczewski antidamping torque, which gives rise to the a-STT in an inhomogeneous magnetic material, is not conservative, and cannot be included in the Lagrangian while the field-like torque, which becomes a na-STT inside a DW, can be.

$\boldsymbol{m}_1$ and $\boldsymbol{m}_2$ are always antiparallel to each other when the field associated with J is much stronger than the external stimulus. One can then use a single order parameter $\boldsymbol{m} = \boldsymbol{m}_1 = -\boldsymbol{m}_2$ to describe the system. ($\theta_1 = \pi - \theta_2 = \theta$, $\phi_1 = \phi_2 + \pi = \phi$, θ, ϕ are the polar angle and azimuthal angle of $\boldsymbol{m}$). The dynamics of $\boldsymbol{m}$ is governed by the following effective LLG equation [30,51–53]:

$$\partial_t \boldsymbol{m} = -\gamma \boldsymbol{m} \times \boldsymbol{H} + \alpha \boldsymbol{m} \times \partial_t \boldsymbol{m} + \boldsymbol{\tau}, \qquad (3)$$

where $\boldsymbol{\tau} = (\boldsymbol{\tau}_1 + \boldsymbol{\tau}_2)/\delta s = -u\partial_z\boldsymbol{m} + \beta u \boldsymbol{m} \times \partial_z \boldsymbol{m}$, $\gamma = \mu_0(M_1 - M_2)/\delta s$, $\delta s = s_1 - s_2$, $\boldsymbol{H} = (M_1\boldsymbol{H}_1 - M_2\boldsymbol{H}_2)/(M_1 - M_2)$, $\alpha = (\alpha_{11}s_1 + \alpha_{22}s_2 - \alpha_{12}s_2\gamma_2/\gamma_1 - \alpha_{21}s_1\gamma_1/\gamma_2)/\delta s$, $P \equiv (P_1 - P_2)$, $u = (P\hbar j)/(2e\delta s)$, and $\beta = (\beta_1 P_1 + \beta_2 P_2)/P$ are the effective STT, the effective gyromagnetic ratio, the net spin angular momentum, the effective field, and the effective Gilbert damping coefficient, the effective spin polarization, the effective spin drift velocity, and the effective nonadiabaticity coefficient, respectively. Note that $\alpha\delta s > 0$ is required by the second law of thermodynamics to ensure the dissipativeness (positive-definite) of the Rayleigh functional $R_\alpha = \frac{\alpha\delta s}{2}\int (\partial_t \boldsymbol{m})^2 d^3\boldsymbol{x}$. The total magnetic energy written in terms of $\boldsymbol{m}$ is $E_\mathrm{m}[\boldsymbol{m}] = \int [A(\nabla \boldsymbol{m})^2 + f(\boldsymbol{m})]d^3\boldsymbol{x}$, with $A = A_1 + A_2$ and $f(\boldsymbol{m}) = f_1(\boldsymbol{m}) + f_2(-\boldsymbol{m})$, then the effective field is given by $\boldsymbol{H} = -[\mu_0(M_1 - M_2)]^{-1}\delta E_\mathrm{m}/\delta \boldsymbol{m}$. γ, $\boldsymbol{\tau}$, and α diverge near the AMCP, $\delta s \to 0$, and a proper limit should be considered in dealing with Eq. (3).

B. Micromagnetic simulations

Throughout this study, all analysis and theoretical results will be verified and compared with numerically solutions of Eq. (2) [not the effective Eq. (3)] obtained by MuMax3 [54] without any approximation for DWs in FiM strip wires as shown in Fig. 1 and explained in the previous section. In our simulations, strip size is $8\,\mathrm{nm} \times 2\,\mathrm{nm} \times 2048\,\mathrm{nm}$. The cell size is chosen to be $1\,\mathrm{nm} \times 1\,\mathrm{nm} \times 0.5\,\mathrm{nm}$. To mimic a rare-earth-transition-metal alloy (such as GdFeCo, GdFe, GdCo) [17,18,20,22,55–59], the model parameters are $J = 109.08\,\mathrm{MJ/m^3}$, $A_1 = A_2 = 1.1 \times 10^{-11}\,\mathrm{J/m}$, where $f_\ell = -K_{\ell,z}m_{\ell,z}^2 + K_{\ell,y}m_{\ell,y}^2$ ($\ell = 1, 2$) is used if not stated otherwise, we choose $K_{1,z} = K_{2,z} = 0.7\,\mathrm{MJ/m^3}$, $K_{1,y} = K_{2,y} = 0.07\,\mathrm{MJ/m^3}$. $\alpha_{11} = \alpha_{22} = 0.01$, $\alpha_{12} = \alpha_{21} = 0$, $P_1 = 0.7$, $P_2 = 0.3$, $M_1 = 1010\,\mathrm{kA/m}$ and $M_2 = 900\,\mathrm{kA/m}$ are assumed if not stated otherwise. The J value is equivalent to hundreds of Tesla to guarantee the antiparallel alignment of spins in two sublattices. Other parameters such as $\beta_1 = \beta_2$, γ_1 and γ_2 can vary in our simulations to mimic and to simulate different FiM wires. In the simulations below, AMCP is modeled by $\gamma_1 M_2/M_1 = \gamma_2 = 1.76 \times 10^{11}\mathrm{s^{-1}T^{-1}}$. Away from the AMCP, $\gamma_1 = \gamma_2 = 1.76 \times 10^{11}\mathrm{s^{-1}T^{-1}}$ are used if not stated otherwise. In terms of parameters in Eq. (3), $P = P_1 - P_2 = 0.4$, $K_z = 1.4\,\mathrm{MJ/m^3}$, and $A = 2.2 \times 10^{-11}\,\mathrm{J/m}$.

In simulations, a DW is first created at the center of nanowire, then an electric current is applied in the $+\hat{z}$ direction. The velocity is obtained from the linear fit of time-evolution curve of the DW center (where $m_z = 0$). For current density above the Walker breakdown, the average velocities are obtained from data accumulated for more than four oscillating periods.

III. RESULTS

A. DW plane twisting by an a-STT

Similar to the well-known result in the ferromagnetic case [5], a static DW is possible under an a-STT below a critical value. A static DW must satisfy $\frac{\delta(E_\mathrm{m}+E_\mathrm{a})}{\delta \boldsymbol{m}} = \boldsymbol{0}$, or

$$\frac{d^2\theta}{dz^2} - \frac{1}{2A}\frac{\partial f}{\partial\theta} - \left(\frac{d\phi}{dz}\right)^2 \sin\theta\cos\theta + \frac{P\hbar j}{4Ae}\frac{d\phi}{dz}\sin\theta = 0, \qquad (4a)$$

$$\frac{d}{dz}\left(\sin^2\theta\frac{d\phi}{dz}\right) - \frac{1}{2A}\frac{\partial f}{\partial\phi} - \frac{P\hbar j}{4Ae}\frac{d\theta}{dz}\sin\theta = 0. \qquad (4b)$$

For simplicity and considering the widely used biaxial model of $f = -K_z\cos^2\theta + K_y\sin^2\theta\sin^2\phi$, Eq. (4) for a small current have a well-known solution of $\phi = \mathrm{const.}$ and $\theta(z) = 2\arctan[\exp(z/\Delta)]$, where $\Delta = \sqrt{A/(K_z + K_y\sin^2\phi)}$ [4,5]. The solution comes from a delicate cancellation of $\partial f/\partial\phi \propto \sin^2\theta$ with the term of $d\theta/dz \propto \sin\theta$ in Eq. (4b). The cancellation occurs at $\phi = \mathrm{const.}$ θ is then determined by Eq. (4a) at a constant ϕ giving by $\Delta\sin 2\phi = \pm\frac{P\hbar j}{2eK_y}$ for j below $j_W = \frac{2e}{P\hbar}\max[\pm K_y\Delta\sin 2\phi]$, "+" ("−") for a TT (HH) DW, respectively.

$\phi = \mathrm{const.}$, or flat DW plane, under an a-STT is only true for the special biaxial model where $\partial f/\partial\phi \propto \sin^2\theta$ and the term of $d\theta/dz \propto \sin\theta$ in Eq. (4b) cancel with each other. For a wire of general magnetic anisotropy, θ and ϕ are coupled, and the Walker solution does not apply. One can only numerically solve Eq. (4). From $E_\mathrm{a} = -\int \frac{P\hbar j}{2e}\phi(\partial_z\cos\theta)d^3\boldsymbol{x}$, the a-STT has a spatially dependent ϕ-component which tends to twist DW plane. The twisting direction depends on the current direction and topological charge density $\rho = -\frac{1}{2}\partial_z\cos\theta$ [14,15]. The integral over z is DW winding angle or DW charge, $Q = \int_{-\infty}^{+\infty}\rho dz = \pm 1$, 1 for a head-to-head (HH) DW and −1 for a tail-to-tail (TT) DW.

To show DW plane twisting, we consider a modified biaxial model of $f = -K_z\cos^2\theta + K_y'\sin^4\theta\sin^4\phi$ in Eq. (4) such that there is no exact cancellation any more. MuMax3 [54]

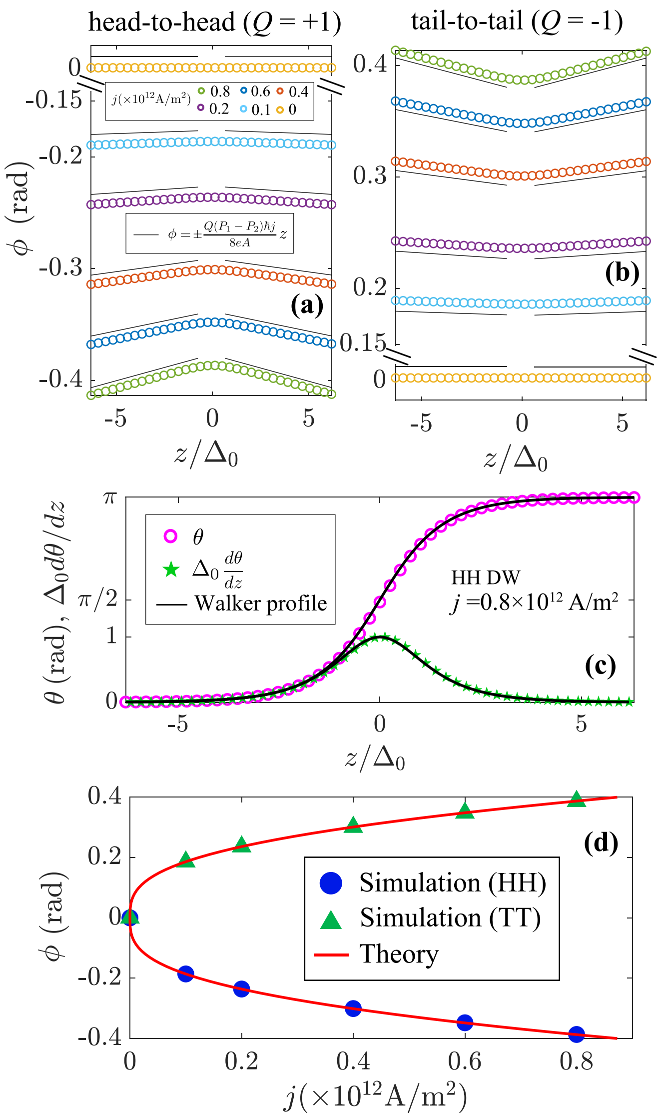

FIG. 2. Distribution of the azimuthal and polar angles of m under different current densities for a HH DW (a) and a TT DW (b). Symbols are simulation results for $j = 0.8$ (green), 0.6 (dark blue), 0.4 (orange), 0.2 (violet), 0.1(light blue), 0 (yellow) in unit of $10^{12}\,\mathrm{A/m^2}$. The black solid lines in panels (a, b) have slopes of $d\phi/dz = \pm QP\hbar j/(8eA)$. (c) $\theta(z)$ and $d\theta/dz$ for a HH DW under a current $j = 0.8\times 10^{12}\,\mathrm{A/m^2}$. Solid line is the Walker profile. (d) ϕ at the DW center as a function of j. The blue dots and green triangles are for a HH and a TT DW, respectively. The red solid line is Eq. (5). $f_l = -K_{l,z}\cos^2\theta_l + K'_{l,y}\sin^4\theta_l\sin^4\phi_l$ with $K'_{1,y} = K'_{2,y} = 0.1\,\mathrm{MJ/m^3}$. $\Delta_0 = 3.96$ nm, $\alpha_{11} = \alpha_{22} = 0.1$ (we use larger damping coefficients to get a static solution more quickly), $\alpha_{12} = \alpha_{21} = 0$, and other material parameters are specified in Sec. II B.

(see Sec. II B for details) is used to numerically solve Eq. (2) in the presence of a-STT. Thus, simulation results can also be used to test how good the approximated Eqs. (3) and (4) are. Starting from a static DW at the center of a nanowire, ϕ_ℓ of the DW is 0 (π) for a HH (TT) DW in the absence of a-STT. An a-STT from various current density given in Fig. 2 is turned on at $t = 0$. In less than 0.5 ns, the DW becomes static again ($\partial_t \boldsymbol{m}_\ell = \mathbf{0}$), showing the existence of a static DW. In terms of variables of Eq. (3), the spatial distribution of ϕ for a HH and a TT DW is shown in Figs. 2(a) and 2(b), respectively. Clearly, spins inside the HH (TT) DW rotate along the wire, either clockwise or counterclockwise. Away from the DW center, the azimuthal angle varies linearly along the wire with a slope of $\pm\frac{QP\hbar j}{8eA}$, indicated by the black solid lines in Figs. 2(a) and 2(b).

For a realistic current density $j = 0.8\times 10^{12}\,\mathrm{A/m^2}$ and effective material parameters of $A = 2.2\times 10^{-11}$ J/m, $P = 0.4$, $K_z = 1.4\,\mathrm{MJ/m^3}$, $\frac{d\phi}{dz}$ is order of $\frac{P\hbar j}{8eA} \sim 1.2\times 10^6\,\mathrm{m^{-1}}$, and $\frac{d\theta}{dz}$ is about $\Delta_0^{-1} = \sqrt{K_z/A} \sim 2.5\times 10^8\,\mathrm{m^{-1}}$. Since $\frac{d^2\theta}{dz^2}, \frac{1}{2A}\frac{\partial f}{\partial\theta} \sim 10^{16}\,\mathrm{m^{-2}}$, and $(\frac{d\phi}{dz})^2\sin\theta\cos\theta$, $\frac{P\hbar j}{4eA}\frac{d\phi}{dz}\sin\theta \sim 10^{12}\,\mathrm{m^{-2}}$, Eq. (4a) is dominated by the first two terms, 4 orders of magnitude larger than the other two terms. $\theta(z)$ is then well approximated by the Walker profile $\theta(z) \simeq 2\arctan[\exp(Qz/\Delta_0)]$, $d\theta/dz \simeq Q\sin\theta/\Delta_0 = Q\,\mathrm{sech}(z/\Delta_0)/\Delta_0$ as shown in Fig. 2(c) with an excellent agreement between the theory (solid lines) and micromagnetic simulations (symbols) of Eq. (2) for $j = 0.8\times 10^{12}\mathrm{A/m^2}$. The good agreements demonstrate that Eq. (4) can well describe the static solutions of Eq. (2). It is worth noting that the spatial variation of ϕ under an a-STT is visible, but very small. Away from DW center, θ is 0 or π, and ϕ is not well defined and has no effect on wire energy and magnetization dynamics.

ϕ at the DW center can also be estimated from energy minimization. Since ϕ does not change much according to analysis above, thus we can express the DW energy $E_\mathrm{m} + E_\mathrm{a}$ as a function of ϕ by integrating over the wire using the Walker profile and constant ϕ. Use $\int_{-\infty}^{+\infty}\sin^2\theta dz = 2\Delta_0$, $\int_{-\infty}^{+\infty}\sin^4\theta dz = \frac{4}{3}\Delta_0$, we have $E_\mathrm{m} + E_\mathrm{a} = S[4\sqrt{AK_z} + \frac{4}{3}\Delta_0 K'_y\sin^4\phi + \frac{QP\hbar j}{e}\phi]$. Minimizing this total energy with respect to ϕ gives us the azimuthal angle at the DW center under applied current density j,

$$\frac{16}{3}\Delta_0 K'_y\sin^3\phi\cos\phi + \frac{QP\hbar j}{e} = 0. \tag{5}$$

Equation (5) [the red solid line in Fig. 2(d)] explains well micromagnetic simulations (dots) as shown in Fig. 2(d).

As shown above, DW plane twisting by an a-STT is general, absent only for a special class of biaxial wires. Although both magnetic field and an a-STT can be incorporated in the Lagrangian as the Zeeman energy functional and E_a, respectively, static fields and a-STTs have very different effects on DWs. A static magnetic field (along $+\hat{z}$) creates an energy density difference between two uniform magnetic domains separated by a DW such that the static DW cannot exist [40,43,44], in contrast, an a-STT changes energy density (E_a) only inside the DW such that a static DW is possible under an a-STT alone and the a-STT tends to twist the DW plane. This twisting occurs only within a DW, thus it should have important implications to DW motion. Results above are general and applicable to other forms of anisotropy, such as cubic anisotropy presented in gadolinium iron garnets [60]; see Appendix C for details.

B. Nonexistence of a static DW under an arbitrarily small na-STT

Two results are presented here. One is that a na-STT cannot be expressed as an energy functional, unlike an a-STT being incorporated into the Lagrangian. Second, a static DW cannot exist in a homogeneous FiM nanowire under an arbitrarily small na-STT. The importance of this na-STT to DW motion in ferromagnetic wires was known for a long time [6,9].

To prove nonexistence of $E_{\mathrm{na},\ell}$ such that $\boldsymbol{m}_\ell \times \frac{\delta E_{\mathrm{na},\ell}}{\delta \boldsymbol{m}_\ell} = \boldsymbol{\tau}_{\mathrm{na},\ell} = \frac{\beta_\ell P_\ell \hbar j}{2e}\boldsymbol{m}_\ell \times \partial_z \boldsymbol{m}_\ell$, we assume that this assertion is incorrect. Then one has $E_{\mathrm{na},\ell} \equiv \int \varepsilon_{\mathrm{na},\ell}(\theta_\ell, \phi_\ell, \partial_z\theta_\ell, \partial_z\phi_\ell)d^3\boldsymbol{x}$ because the na-STT depends on $\boldsymbol{m}_\ell$ and $\partial_z\boldsymbol{m}_\ell$. In the local coordinate system of $(\boldsymbol{e}_{\boldsymbol{m}_\ell}, \boldsymbol{e}_{\theta_\ell}, \boldsymbol{e}_{\phi_\ell})$, one has

$$\frac{\partial \varepsilon_{\mathrm{na},\ell}}{\partial \theta_\ell} - \partial_z\left(\frac{\partial \varepsilon_{\mathrm{na},\ell}}{\partial(\partial_z\theta_\ell)}\right) = \frac{\beta_\ell P_\ell \hbar j}{2e}\partial_z\theta_\ell, \tag{6a}$$

$$\frac{\partial \varepsilon_{\mathrm{na},\ell}}{\partial \phi_\ell} - \partial_z\left(\frac{\partial \varepsilon_{\mathrm{na},\ell}}{\partial(\partial_z\phi_\ell)}\right) = \frac{\beta_\ell P_\ell \hbar j}{2e}\partial_z\phi_\ell \sin^2\theta_\ell. \tag{6b}$$

Equation (6a)$\times\partial_z\theta_\ell +$ Eq. (6b)$\times\partial_z\phi_\ell$ and integrate over z, we have

$$\left[\varepsilon_{\mathrm{na},\ell} - \frac{\partial \varepsilon_{\mathrm{na},\ell}}{\partial(\partial_z\theta_\ell)}\partial_z\theta_\ell - \frac{\partial \varepsilon_{\mathrm{na},\ell}}{\partial(\partial_z\phi_\ell)}\partial_z\phi_\ell\right]\Bigg|_{z=-\infty}^{z=+\infty} = \frac{\beta_\ell P_\ell \hbar j}{2e}\int_{-\infty}^{+\infty}(\partial_z\boldsymbol{m}_\ell)^2 dz. \tag{7}$$

$(\partial_z\theta_\ell)^2 + (\partial_z\phi_\ell \sin\theta_\ell)^2 = (\partial_z\boldsymbol{m}_\ell)^2$ is used above. Applying Eq. (7) to a wire with two DWs such that two domains on the far left and the far right are the same, i.e., $\varepsilon_{\mathrm{na},\ell}(z=-\infty) = \varepsilon_{\mathrm{na},\ell}(z=+\infty)$, the left-hand side (LHS) of Eq. (7) vanishes while the right-hand side (RHS) of Eq. (7) is nonzero and positive definite because of the contributions from the DWs in the wire. Thus, the assumption of existence of $E_{\mathrm{na},\ell}$ cannot be true. The similar conclusion was also made in a recent work from collective coordinate assumption and introduction of an artificially charge [62].

To show nonexistence of a static DW in the presence of an arbitrarily small na-STT, let us assume Eq. (2) have time-independent solution ($\partial_t\boldsymbol{m}_1 = \partial_t\boldsymbol{m}_2 = \boldsymbol{0}$) such that the left-hand sides of Eq. (2), as well as the second and the third terms in the brackets on the right-hand sides, are zeros. In the coordinate of $(\boldsymbol{e}_{\boldsymbol{m}_\ell}, \boldsymbol{e}_{\theta_\ell}, \boldsymbol{e}_{\phi_\ell})$, the $\boldsymbol{e}_{\theta_\ell}$ and $\boldsymbol{e}_{\phi_\ell}$ components of Eq. (2) become

$$\frac{\delta E_{\mathrm{m}}}{\delta \theta_\ell} = -\tau_{\phi,\ell}, \tag{8a}$$

$$\frac{\delta E_{\mathrm{m}}}{\delta \phi_\ell} = \tau_{\theta,\ell}\sin\theta_\ell \tag{8b}$$

where $\ell = 1, 2$ labels two sublattices. For quasi-1D nanowires of a uniform spin distribution in the xy-plane, i.e. $\partial_x\boldsymbol{m}_\ell = \partial_y\boldsymbol{m}_\ell = \boldsymbol{0}$, one has $\int d^3\boldsymbol{x} = S\int dz$, where S is the cross-section area of the nanowire. $\partial_z\theta_\ell \times$ Eq. $(8a) + \partial_z\phi_\ell \times$ Eq. $(8b)$, summing over ℓ and integrating over z, we obtain, by using $\tau_{\theta,\ell} = -\frac{P_\ell \hbar j}{2e}\partial_z\theta_\ell - \frac{\beta_\ell P_\ell \hbar j}{2e}\sin\theta_\ell\partial_z\phi_\ell$, $\tau_{\phi,\ell} = -\frac{P_\ell \hbar j}{2e}\sin\theta_\ell\partial_z\phi_\ell + \frac{\beta_\ell P_\ell hbar j}{2e}\partial_z\theta_\ell$ and after some algebra,

$$S\int_{-\infty}^{+\infty}\frac{d\varepsilon_{\mathrm{m}}}{dz}dz = -S\sum_{\ell=1,2}\frac{\beta_\ell P_\ell \hbar j}{2e}\int_{-\infty}^{+\infty}(\partial_z\boldsymbol{m}_\ell)^2 dz. \tag{9}$$

The LHS of Eq. (9) is zero since $S[\varepsilon_{\mathrm{m}}(z=+\infty) - \varepsilon_{\mathrm{m}}(z=-\infty)]$, while the RHS is nonzero unless $\beta_\ell = 0$ due to the spin variations inside the DW. Thus, Eq. (9) cannot be true and a static DW cannot exist in the presence of a na-STT. A DW must move under an arbitrarily small na-STT.

C. Energy-work principle and DW velocity

Since a DW must move under a na-STT which does a positive work, the energy-work principle says that the power done by STTs should equal to the sum of the dissipated power during the DW motion and the magnetic energy changing rate. Approximating Eq. (2) by Eq. (3), the magnetic energy changing rate is $\frac{dE_{\mathrm{m}}}{dt} = \int \frac{\delta E_{\mathrm{m}}}{\delta \boldsymbol{m}}\cdot\partial_t\boldsymbol{m}d^3\boldsymbol{x} = \mu_0(M_1 - M_2)\int -\boldsymbol{H}\cdot\partial_t\boldsymbol{m}d^3\boldsymbol{x}$. Operate $\partial_t\boldsymbol{m}\cdot(\boldsymbol{m}\times\cdots)$ on both sides of Eq. (3), one has the LHS equal to zero, and solving RHS $= 0$ for $\boldsymbol{H}\cdot\partial_t\boldsymbol{m}$ gives $\boldsymbol{H}\cdot\partial_t\boldsymbol{m} = \gamma^{-1}[\alpha(\partial_t\boldsymbol{m})^2 - \partial_t\boldsymbol{m}\cdot(\boldsymbol{m}\times\boldsymbol{\tau})]$. Substitute it to the expression of $\frac{dE_{\mathrm{m}}}{dt}$ above, the first term gives the energy dissipation rate, and the second term gives power supplied by the a-STT and na-STT when the corresponding STTs in $\boldsymbol{\tau}$ are used. Interestingly, instead of scalar product of torque with the angular velocity as the power done by a torque on a Newtonian rigid-body with inertial, the power done by a torque on the spin angular momentum governed by the LLG equation is proportional to $\partial_t\boldsymbol{m}\cdot(\boldsymbol{m}\times\boldsymbol{\tau})$. With some algebra, the energy change rate equal to the sum of dissipative power and powers from the a-STT and na-STT,

$$\frac{dE_{\mathrm{m}}}{dt} = \mathcal{P}_\alpha + \mathcal{P}_{\mathrm{na}} + \mathcal{P}_{\mathrm{a}}. \tag{10}$$

The dissipative power is

$$\begin{aligned}\mathcal{P}_\alpha = -2R_\alpha &= -\alpha\delta s\int(\partial_t\boldsymbol{m})^2 d^3\boldsymbol{x}\\ &= -\frac{\delta s\alpha}{(1+\alpha^2)}\int[(\gamma H_\phi + \tau_\theta)^2\\ &\quad + (\gamma H_\theta - \tau_\phi)^2]d^3\boldsymbol{x},\end{aligned} \tag{11}$$

the power by the na-STT is the Rayleigh functional of the na-STT,

$$\mathcal{P}_{\mathrm{na}} = -R_{\mathrm{na}} = -\delta su\beta\int(\partial_t\boldsymbol{m}\cdot\partial_z\boldsymbol{m})d^3\boldsymbol{x}, \tag{12}$$

and the power by the a-STT is

$$\mathcal{P}_{\mathrm{a}} = \delta su\int\boldsymbol{m}\cdot(\partial_t\boldsymbol{m}\times\partial_z\boldsymbol{m})d^3\boldsymbol{x}. \tag{13}$$

Equation (10) is applicable to any magnetic texture described by the LLG equation. If one uses total energy $E = E_{\mathrm{m}} + E_{\mathrm{a}} = \int[(\sum_{q=\theta_\ell,\phi_\ell}^{\ell=1,2}\frac{\partial\mathcal{L}}{\partial(\partial_t q)}\partial_t q) - \mathcal{L}]d^3\boldsymbol{x}$, then the energy-work relation becomes $\frac{dE}{dt} = -2R_\alpha - R_{\mathrm{na}}$ since $dE_{\mathrm{a}}/dt = -\mathcal{P}_{\mathrm{a}}$. It is equivalent to use either E or E_{m}. Equation (10) was known before [5,10], but was not used to understand DW motion.

To connect the energy-work principle to DW motion and to be specific, we consider a HH DW in the widely studied biaxial wires, $f = -K_z\cos^2\theta + K_y\sin^2\theta\sin^2\phi$. Rewrite Eq. (3) in terms of θ, ϕ,

$$(1+\alpha^2)\partial_t\theta = \gamma H_\phi + \alpha\gamma H_\theta + \tau_\theta - \alpha\tau_\phi, \tag{14a}$$

$$(1+\alpha^2)\partial_t\phi\sin\theta = \alpha\gamma H_\phi - \gamma H_\theta + \alpha\tau_\theta + \tau_\phi, \tag{14b}$$

with $H_\theta = \frac{1}{\mu_0(M_1-M_2)}[2A\frac{\partial^2\theta}{\partial z^2} - \frac{\partial f}{\partial \theta} - 2A\sin\theta\cos\theta(\frac{\partial\phi}{\partial z})^2]$ and $H_\phi = -\frac{1}{\mu_0(M_1-M_2)\sin\theta}\frac{\partial f}{\partial\phi} + \frac{2A}{\mu_0(M_1-M_2)\sin\theta}\frac{\partial}{\partial z}(\sin^2\theta\frac{\partial\phi}{\partial z})$.

For $j < j_W$ discussed below, one can verify that $\theta[(z-vt)/\Delta] = 2\arctan\{\exp[(z-vt)/\Delta]\}$ and $\phi = \text{const.}$, with $v = \beta u/\alpha$ and $\Delta = \sqrt{\frac{A}{K_z + K_y\sin^2\phi}}$, are exact solutions of Eq. (14) with $\tau_\theta = -u\partial_z\theta$, $\tau_\phi = \beta u\partial_z\theta$, and $\frac{\partial f}{\partial\theta} = 2\sin\theta\cos\theta(K_z + K_y\sin^2\phi)$. The solution has $\partial_z\theta = \sin\theta/\Delta$ and $\partial_{zz}\theta = (\cos\theta/\Delta)\partial_z\theta = \sin\theta\cos\theta/\Delta^2$, $2A\partial_{zz}\theta - \partial f/\partial\theta = 0$, and $\partial_z\phi = 0$ such that $H_\theta = 0$.

From these conditions, Eq. (14b) becomes

$$\partial_t\phi = \frac{1}{\delta s(\alpha^2+1)}\left(\frac{\beta_1P_1 + \beta_2P_2 - \alpha P}{\Delta}\frac{\hbar j}{2e} - \alpha K_y\sin 2\phi\right). \tag{15}$$

The rigid-body motion requires $\partial_t\phi = 0$, and Eq. (15) can only be true when j is smaller than the Walker breakdown current density $j_W = \frac{2e}{\hbar}\max[\frac{\alpha K_y\Delta\sin 2\phi}{\beta_1P_1+\beta_2P_2-\alpha P}]$. j_W does not diverge at AMCP ($\delta s = 0$ and $\alpha \to \infty$) unless $P = 0$ or $P_1 = P_2$. This result differs from the absence of Walker breakdown at AMCP for field-driven DW motion [17,40]. We will see below that this difference leads to unique dynamical behaviors of current-driven FiM DW motion around AMCP. The energy-work relation in the rigid-body motion ($j < j_W$) is $\mathcal{P}_\alpha + \mathcal{P}_{\text{na}} = 0$ since $dE/dt = 0$. The physical picture of this relation is clear: The power of na-STT overcomes the dissipation power caused by DW motion to maintain a constant DW speed. Putting $\partial_t\phi = 0$ and $H_\theta = 0$ into Eq. (14b), one has $\gamma H_\phi = -(\alpha\tau_\theta + \tau_\phi)/\alpha$. Substitute these expressions into Eq. (11), one obtains $\mathcal{P}_\alpha = -\delta s(\beta^2u^2/\alpha)\int(\partial_z\theta)^2dz$. Substitute $\partial_t\boldsymbol{m}\cdot\partial_z\boldsymbol{m} = \partial_t\theta\partial_z\theta = -v(\partial_z\theta)^2$ into Eq. (12), one has $\mathcal{P}_{\text{na}} = \delta s v\beta u\int(\partial_z\theta)^2dz$. Combining these results with $\mathcal{P}_\alpha + \mathcal{P}_{\text{na}} = 0$, we derived the well known DW velocity of $v = \beta u/\alpha$. In terms of model parameters used in Eq. (2), DW velocity is

$$v = \frac{\beta_1P_1 + \beta_2P_2}{\alpha\delta s}\frac{\hbar j}{2e}. \tag{16}$$

For $j > j_W$, a DW precesses around the nanowire axis as it propagates along the wire. The magnetic energy of the DW oscillates with time because the DW experiences different magnetic anisotropy, resulting in the variation of the DW width.

Of course, the long time-averaged DW energy changing rate is zero because the DW energy varies in a narrow range. Interestingly, Eq. (14) can still approximately describe a propagating DW [5] (numerical verification is provided in Appendix B), $\theta(z,t) = 2\arctan\{\exp[(z - \int_0^t v(t')dt')/\Delta(t)]\}$ and $\phi = \phi(t)$, where $\Delta(t) = \sqrt{\frac{A}{K_z + K_y\sin^2\phi(t)}}$ is the DW width. Then $H_\theta \simeq 0$, $H_\phi \simeq -\frac{K_y\sin 2\phi\sin\theta}{\mu_0(M_1-M_2)}$. Under these approximations (see Appendices A and B for detailed derivations and validations), the power from the na-STT is $\mathcal{P}_{\text{na}} = 2Su\delta s\beta v(t)/\Delta(t)$. Thus $v(t)$ is proportional to $\mathcal{P}_{\text{na}}\Delta(t)$, instead of $\mathcal{P}_{\text{na}}$. To evaluate $\bar{v}$, where the bar denotes the long-time average, we thus multiply both sides of Eq. (10) by Δ, and take the time average such that $\overline{\mathcal{P}_{\text{na}}\Delta} = 2Su\delta s\beta\bar{v}$. The energy-work relation becomes $\overline{\Delta dE_{\text{m}}/dt} = \overline{\mathcal{P}_\alpha\Delta} + \overline{\mathcal{P}_{\text{na}}\Delta} + \overline{\mathcal{P}_{\text{a}}\Delta}$, or equivalently,

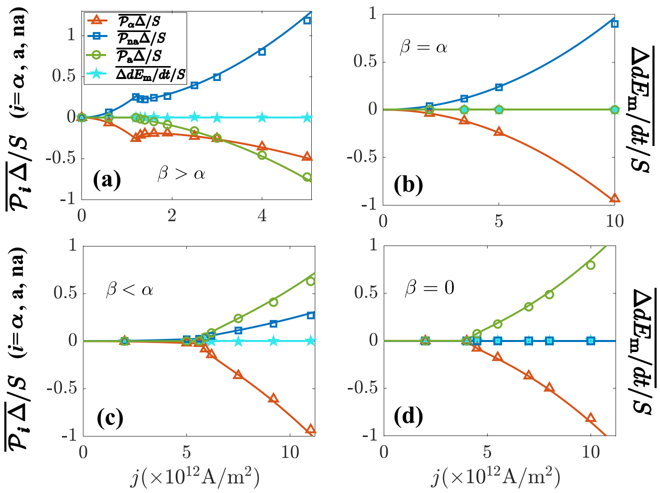

FIG. 3. j-dependencies of $\overline{\mathcal{P}_\alpha\Delta}/S$ (orange), $\overline{\mathcal{P}_{\text{na}}\Delta}/S$ (blue), $\overline{\mathcal{P}_{\text{a}}\Delta}/S$ (green), and $\overline{\Delta dE_{\text{m}}/dt}$ (cyan) for $\beta_1 = \beta_2$=0.3 (a), 0.0695 (b), 0.02 (c), and 0 (d), $\alpha_{11} = \alpha_{22} = 0.01$, $\alpha_{12} = \alpha_{21} = 0$. Symbols are MuMax3 simulations of Eq. (2) and curves are Eq. (18) (red), $\overline{\mathcal{P}_{\text{na}}\Delta}/S = 2u\delta s\beta\bar{v}$ (blue), Eq. (19) (green), and $\overline{\Delta dE_{\text{m}}/dt} = 0$ (cyan). The Walker breakdown current densities are $j_W = 1.24$ (a), $+\infty$ (b), 5.77 (c), 4.11 and (d) $\times 10^{12}$ A/m^2. The effective parameters are calculated as $\alpha = 0.1736$ and $\beta = 0.75 > \alpha$ (a), $\beta = \alpha$ (b), $\beta = 0.05 < \alpha$ (c), and $\beta = 0$ (d). Other parameters for each sublattice are the same as those given in Sec. II B.

$$2Su\delta s\beta\bar{v} = \overline{\Delta dE_{\text{m}}/dt} - \overline{\mathcal{P}_\alpha\Delta} - \overline{\mathcal{P}_{\text{a}}\Delta}. \tag{17}$$

$\overline{\Delta dE_{\text{m}}/dt} = 0$ because $E_{\text{m}} = 4AS/\Delta(t)$ and $\Delta dE_{\text{m}}/dt = -4AS[d\ln(\Delta/\Delta_0)/dt]$. The other two terms on the RHS of Eq. (17) can be expressed as follows, after employing proper approximations discussed in Appendices A and B,

$$\overline{\mathcal{P}_\alpha\Delta} = 2Su\delta s\left(-\frac{\beta^2u}{\alpha} + \frac{(\beta^2-\alpha^2)}{\alpha(1+\alpha^2)}\sqrt{u^2-u_W^2}\right), \tag{18}$$

and

$$\overline{\mathcal{P}_{\text{a}}\Delta} = -2Su\delta s\overline{\Delta\partial_t\phi} = -2Su\delta s\frac{(\beta-\alpha)}{(1+\alpha^2)}\sqrt{u^2-u_W^2}, \tag{19}$$

where $u_W = (P\hbar j_W)/(2e\delta s)$ is u at j_W. The analytical expressions of $\overline{\mathcal{P}_\alpha\Delta}$, $\overline{\mathcal{P}_{\text{na}}\Delta}$, $\overline{\mathcal{P}_{\text{a}}\Delta}$, and $\overline{\Delta dE_{\text{m}}/dt}$, based on spin dynamics of Eq. (3) are verified by MuMax3 simulations on Eq. (2) as shown in Fig. 3. From Eq. (17), the averaged DW velocity $\bar{v}$ is

$$\bar{v} = \frac{\beta}{\alpha}u - \frac{(\beta-\alpha)}{\alpha(1+\alpha^2)}\sqrt{u^2-u_W^2}. \tag{20}$$

In terms of current density, it is

$$\bar{v} = \mu_1 j + \mu_2\left(j - \sqrt{j^2 - j_W^2}\right), \tag{21}$$

where

$$\mu_1 = \frac{P + \alpha(\beta_1P_1 + \beta_2P_2)}{\delta s(1+\alpha^2)}\frac{\hbar}{2e}, \tag{22a}$$

is the asymptotic DW mobility for $j \gg j_W$, and

$$\mu_2 = \frac{(\beta - \alpha)P}{\alpha\delta s(1+\alpha^2)}\frac{\hbar}{2e} \tag{22b}$$

is a correction to DW mobility above the Walker breakdown current. An interesting observation is that, although Eq. (21) is obtained for the case of $j > j_W$, result for $j < j_W$ is the real part of Eq. (21), namely $\bar{v} = (\mu_1 + \mu_2)j = \frac{\beta_1 P_1 + \beta_2 P_2}{\alpha\delta s}\frac{\hbar}{2e}j$.

Equations (18)–(20) derived from the energy-work relations in the precessional regime ($j > j_W$) are beyond the collective mode theory. Without the loss of generality, we assume $j > 0$, $P > 0$, and $\delta s > 0$. On the one hand, work done by a na-STT is always nonzero and positive. On the other hand, an a-STT can do either negative or positive work, depending on the direction of the DW precession, or the sign of $\partial_t\phi$. (1) When $\beta > \alpha$, the DW plane precesses right-handedly ($\partial_t\phi > 0$), a-STT does a negative work [Fig. 3(a)]. (2) When $\beta = \alpha$ ($\partial_t\phi = 0$), the DW does not precess, and the a-STT does no work [Fig. 3(b)]. (3) When $\beta < \alpha$ ($\partial_t\phi < 0$), the a-STT does a positive work [Fig. 3(c)].

In the absence of a na-STT ($\beta = 0$), the work done by the a-STT in the precessional regime must be dissipated by the damping through DW propagation along the wire as revealed in Fig. 3(d). The $\boldsymbol{e}_\phi$ component of Eq. (3) is $\sin\theta\partial_t\phi = -\gamma H_\theta + \alpha\partial_t\theta + \tau_\phi$. Multiply both sides of the equation by $\sin\theta$ and integrate over z, the left-hand side is $2\Delta\partial_t\phi$ because of $\int\sin^2\theta dz = 2\Delta$. The second term on the right-hand side is $-2\alpha v$ because $\theta(z,t) = 2\arctan\{\exp[(z - \int_0^t v(t')dt')/\Delta(t)]\}$ leads to $v = -0.5\int\sin\theta\partial_t\theta dz$. The first and third terms on the right-hand side vanish because $H_\theta = 0$ and $\tau_\phi = -u\sin\theta\partial_z\phi = 0$ (since $\partial_z\phi$ is negligible, see Appendices A and B). After taking the long-time average, one has $\alpha\bar{v} = -\overline{\Delta\partial_t\phi}$. From $\overline{\Delta\partial_t\phi}$ given in Eq. (19), the average DW speed is $\bar{v} = \frac{1}{1+\alpha^2}\sqrt{u^2 - u_W^2}$, the same as Eq. (20) for $\beta = 0$.

Figure 4(a) shows current density dependence of DW speed in a wire away from the AMCP. Symbols are MuMax3 simulations of Eqs. (2) and curves are Eq. (16) for $j < j_W$ and Eq. (21) for $j > j_W$. The excellent agreements demonstrate again the good approximation of Eq. (3) by Eq. (2), as well as the accuracy of our analysis. In summary, Eq. (20) [or equivalently Eq. (21)] is applicable to current density, both below and above the Walker breakdown.

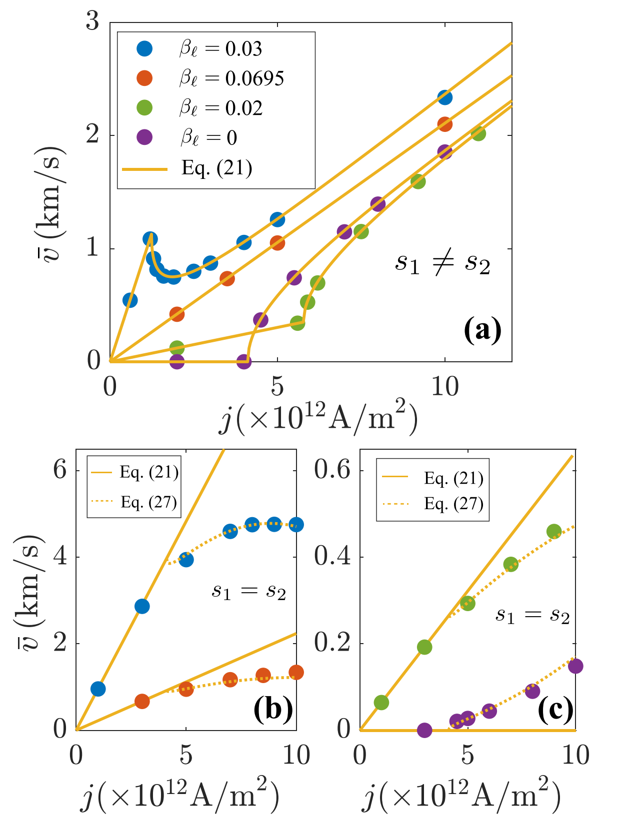

FIG. 4. Current-density dependencies of averaged DW velocity for a nanowire away from the AMCP (a) and at AMCP (b), (c). An AMCP is modelled by $\gamma_1 M_2/M_1 = \gamma_2 = 1.76 \times 10^{11}\mathrm{s^{-1}T^{-1}}$. Away from the AMCP, $\gamma_1 = \gamma_2 = 1.76 \times 10^{11}\mathrm{s^{-1}T^{-1}}$ are used. The symbols are MuMax3 simulations on Eq. (2), the yellow solid curves are Eq. (16) (for $j < j_W$) and (21) (for $j > j_W$), and the yellow dashed curves in panels (b), (c) are prediction of Eq. (27). Model parameters are $\alpha_{11} = \alpha_{22} = 0.01$, $\alpha_{12} = \alpha_{21} = 0$, $\beta_1 = \beta_2 = 0.3$ (blue), 0.0695 (orange), 0.02 (green), and 0 (violet), respectively. The effective parameters calculated from sublattice parameters in panel (a) are $\alpha = 0.1736$, and $\beta = 0.75 > \alpha$ (blue), $\beta = \alpha$ (orange), $\beta = 0.05 < \alpha$ (green), and $\beta = 0$ (violet), respectively. While α in panels (b), (c) diverges since it is at AMCP. Other parameters for each sublattice are the same as those given in Sec. II B.

D. DW velocity around AMCP

j_W does not diverge at AMCP ($\delta s = 0$) in general, unless $P_1 = P_2$ ($P = 0$). Thus, the Walker breakdown occurs even at the AMCP, in contrast to the absence of the Walker breakdown ($H_W = \infty$) at AMCP for field-driven DW motion. For $j > j_W$, DW precession velocity $\partial_t\phi$ is proportional to $\frac{\alpha}{\delta s(1+\alpha^2)}$ according to Eq. (15). The limit of $\partial_t\phi$ under $\delta s \to 0$ ($\alpha \to \infty$) is finite and reaches its maximal value. Thus, a DW precesses at a high velocity of $\partial_t\phi \sim -P\hbar j/(2e\delta s\alpha\Delta)$ at the AMCP. The high precession is mainly caused by the a-STT, consistent with the fact that the energy of the a-STT prefers a smaller ϕ for a HH DW. Although Eq. (21) predicts no change in DW mobility beyond the Walker breakdown at the AMCP, a high precession can lead to a significant DW structure change, and a time-dependent DW deformation emits spin waves during the DW propagation. The DW deformation and spin wave emissions invalidates most of the approximations used in previous analysis. Six videos in the Supplemental Material [61] show strong spin wave emission around the AMCP when the applied current is above the Walker breakdown current (Videos 1–4) and negligible spin wave emission away from the AMCP and above the Walker breakdown (Videos 5 and 6). The simulation setup in the videos are the same as that in Sec. II B and Fig. 4.

However, the effective LLG equation [Eq. (3)] is still valid. We extract the $\phi_1, \phi_2 + \pi$, components of $\boldsymbol{m}_1, \boldsymbol{m}_2$ from simulation done for the nanowire at AMCP with $\beta_1 = \beta_2 = 0.3$, $\alpha_{11} = \alpha_{22} = 0.01$, $\alpha_{12} = \alpha_{21} = 0$. $\gamma_1 M_2/M_1 = \gamma_2 = 1.76 \times 10^{11}\mathrm{s^{-1}T^{-1}}$. The current density is $j = 5 \times 10^{12}\mathrm{A/m^2} > j_W = 4.1 \times 10^{12}\mathrm{A/m^2}$. Other material parameters are specified in Sec. II B. We plot $\phi_1, \phi_2 + \pi$, and components of

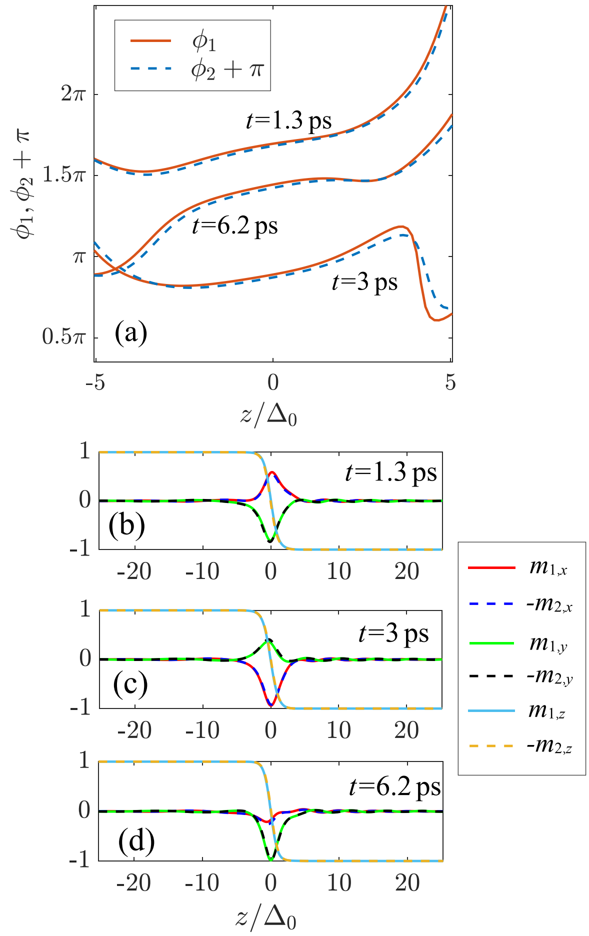

FIG. 5. Azimuthal angles ϕ_1, ϕ_2 and components of $\boldsymbol{m}_1$, $\boldsymbol{m}_2$ at three different moments $t = 1.3, 3, 6.2$ ps obtained from simulation done for the nanowire at AMCP with $\beta_1 = \beta_2 = 0.3$, $\alpha_{11} = \alpha_{22} = 0.01$, $\alpha_{12} = \alpha_{21} = 0$. $\gamma_1 M_2/M_1 = \gamma_2 = 1.76\times 10^{11}\,\mathrm{s^{-1}T^{-1}}$. The current density is $j = 5\times 10^{12}\,\mathrm{A/m^2} > j_W = 4.1\times 10^{12}\,\mathrm{A/m^2}$. Other material parameters are specified in Sec. II B. The solid lines in panel (a) are ϕ_1 while the dashed lines are the $\phi_2+\pi$. In (b)–(d), the red, green, and light blue solid lines are the $m_{1,x}$, $m_{1,y}$, and $m_{1,z}$, while the blue, black, and yellow dashed lines are the $-m_{2,x}$, $-m_{2,y}$, and $-m_{2,z}$.

$\boldsymbol{m}_1, \boldsymbol{m}_2$ (at the middle of the column of the films for each given z) as functions of z in Fig. 5. The overlap between solid and dashed lines verifies the validity of Eq. (3).

Now we generalize Eq. (21) to the case of DW deformation [yellow solid lines and color dots in Figs. 4(b) and 4(c)]. Let us rewrite Eq. (3) as

$$\delta s\partial_t \boldsymbol{m} = \boldsymbol{m}\times\frac{\delta E_\mathrm{m}}{\delta \boldsymbol{m}} + \alpha\delta s\boldsymbol{m}\times\partial_t\boldsymbol{m} - \frac{P\hbar j}{2e}\partial_z\boldsymbol{m} + \frac{\beta P\hbar j}{2e}\boldsymbol{m}\times\partial_z\boldsymbol{m}. \tag{23}$$

At AMCP, $\delta s = 0$, the LHS of Eq. (23) vanishes. $\int dz\{\partial_z\boldsymbol{m}\cdot[\boldsymbol{m}\times \text{Eq. (23)}]\}$ yields

$$\alpha\delta s\int \partial_z\boldsymbol{m}\cdot\partial_t\boldsymbol{m}dz + \frac{\beta P\hbar j}{2e}\int(\partial_z\boldsymbol{m})^2dz = 0. \tag{24}$$

One may note that $\alpha\delta s$ is not zero. The first and third term on the RHS of Eq. (23) vanish since $\int dz\{\partial_z\boldsymbol{m}\cdot[\boldsymbol{m}\times(\boldsymbol{m}\times\frac{\delta E_\mathrm{m}}{\delta\boldsymbol{m}})]\} = -[\varepsilon_\mathrm{m} - \frac{\partial\varepsilon_\mathrm{m}}{\partial(\partial_z\theta)}\partial_z\theta - \frac{\partial\varepsilon_\mathrm{m}}{\partial(\partial_z\phi)}\partial_z\phi]|_{z=-\infty}^{z=+\infty} = 0$, and $\int dz[\partial_z\boldsymbol{m}\cdot(\boldsymbol{m}\times\partial_z\boldsymbol{m}) = 0$. The DW velocity can be found from the ansatzes of $\theta(z,t) = \theta(z-\int_0^t v(t')dt')$, $\phi(z,t) = \Phi(z-\int_0^t v(t')dt') + \omega t$ [10,26], where Φ describes DW-plane twisting and DW distortion. ω is the rotation velocity of the spin at DW center. Using $\partial_t\theta = -v\partial_z\theta$, $\partial_t\phi = -v\partial_z\Phi + \omega$, $\partial_z\phi = \partial_z\Phi$, one obtains $\partial_z\boldsymbol{m}\cdot\partial_t\boldsymbol{m} = \partial_z\theta\partial_t\theta + \partial_z\phi\partial_t\phi\sin^2\theta = -v[(\partial_z\theta)^2 + (\sin\theta\partial_z\Phi)^2] + \omega\sin^2\theta\partial_z\Phi$, $\partial_z\boldsymbol{m}\cdot\partial_z\boldsymbol{m} = (\partial_z\theta)^2 + (\sin\theta\partial_z\Phi)^2$. The time-averaged DW velocity is

$$\bar{v} = \frac{\beta P\hbar j}{2e\alpha\delta s} + \overline{\left\{\frac{\omega\int\sin^2\theta\partial_z\Phi dz}{\int[(\partial_z\theta)^2 + (\sin\theta\partial_z\Phi)^2]dz}\right\}}. \tag{25}$$

To further simplify the second term on the RHS, we write $\int\sin^2\theta\partial_z\Phi dz = 2\Delta\Phi_z$ and assume $\Phi_z = \partial_z\phi(z)|_{z=0}$, derivative of ϕ at the DW center. Also, $\int[(\partial_z\theta)^2 + (\sin\theta\partial_z\Phi)^2]dz \simeq 2/\Delta$, then $\overline{\{\frac{\omega\int\sin^2\theta\partial_z\Phi dz}{\int[(\partial_z\theta)^2+(\sin\theta\partial_z\Phi)^2]dz}\}} \simeq \overline{\omega\Delta}\,\overline{\Delta\Phi_z}$, so the DW velocity becomes

$$\bar{v} = \frac{\beta P}{\alpha\delta s}\frac{\hbar j}{2e} + \overline{\omega\Delta}\,\overline{\Delta\Phi_z}. \tag{26}$$

We will make a few remarks on Eq. (26) before proceeding further. The second term on the RHS of Eq. (26) is purely caused by the a-STT. Although the a-STT is not explicitly included in Eq. (24), it still has a significant effect on DW dynamics by inducing a high DW precession of ω and by distorting the DW structure ($\overline{\Delta\Phi_z}$). As a result, the DW velocity deviates from a linear relation to the current density, in sharp contrast to the field-driven case, where DW velocity is proportional to the external field strength. The reason for this difference lies in the fact that the STT has both adiabatic and nonadiabatic components, whereas a static external magnetic field exerts only a precessional torque on the spins.

One can estimate the DW precession frequency as $\overline{\omega\Delta} \simeq -\frac{(P_1-P_2)}{\alpha\delta s}\frac{\hbar j}{2e}$. The relation between DW twisting $\overline{\Delta\Phi_z}$ and current density is too complicated to derive analytically, so we fit $\overline{\Delta\Phi_z}$ to $c\sqrt{j^2-j_W^2}$, where c is a fitting parameter measuring the degree of DW twisting, $c=0$ for no twisting. Substituting these expressions into Eq. (26), an approximate formula for DW velocity ($j > j_W$) is obtained,

$$\bar{v} = \frac{\beta P}{\alpha\delta s}\frac{\hbar j}{2e} - c\frac{P}{\alpha\delta s}\frac{\hbar j}{2e}\sqrt{j^2-j_W^2}. \tag{27}$$

In our simulations below, $\beta_1 = \beta_2$ and $\alpha_{11} = \alpha_{22}$ are used. By fitting DW structure data obtained from simulations (see Sec. III E for details), we obtained $c = 1.46\times 10^{-13}(\beta_\ell - \alpha_{\ell\ell})\,\mathrm{m^2/A}$. We compared our theoretical predictions [Eq. (27), the yellow dashed lines in Fig. 4] with MuMax3 simulations (the colored dots) in Figs. 4(b) and 4(c). These results demonstrate that our theory provides an accurate prediction of DW velocity at AMCP.

Our theory provides a novel theoretical explanation to the current-driven DW motion in FiMs at AMCP. No unphysical negative na-STT is used, and the long-standing problem in the field [20,28–32] is solved. DW velocity at AMCP observed in simulations and experiments [20,29] can perfectly explained by the DW deformation.

E. Comparison of simulations with theory for DW twisting at the AMCP

To test how good Eq. (27) is for the velocity of a twisted DW at the AMCP, we carry out simulations for $\alpha_{11} = \alpha_{22} = 0.01$ and four different nonadiabaticities $\beta_1 = \beta_2 = 0.3, 0.0695, 0.02, 0$. $\gamma_1 M_2/M_1 = \gamma_2 = 1.76 \times 10^{11}\,\mathrm{s^{-1}T^{-1}}$ is used to simulate the AMCP while all other parameters for each sublattice are the same as those given in Sec. II B.

The DW structures $\theta_\ell(x, z, n\delta t)$ and $\phi_\ell(x, z, n\delta t)$ ($\ell = 1, 2$) are recorded every δt=0.1 ps for a duration of 20 ps ($n = 1, 2, .., 200$). The average polar and azimuthal angles along the z direction are defined as $\theta_\ell(z, t) = \frac{1}{8}\sum_{x=1,2,...,8}\theta_\ell(x, z, t)$ and $\phi_\ell(z, t) = \frac{1}{8}\sum_{x=1,2,...,8}\phi_\ell(x, z, t)$. The spatial derivatives of ϕ_ℓ along z direction are defined as $\partial_z\phi_\ell = \frac{\phi_\ell(z,t)-\phi_\ell(z-\delta z,t)}{\delta z}$ with $\delta z = 0.5$ nm. Only $\partial_z\phi_\ell(z, t)$ within $[z_0 - 5\Delta_0, z_0 + \Delta_0]$ are collected since $\partial_z\phi_\ell(z, t)$ outside this range is not well defined. We use $\int \sin^2\theta_\ell dz = 2\Delta_\ell$ to calculate $\Delta_\ell(t)$, $\Delta_\ell(t) = 0.5\delta z\sum_{n_1=1,2...,4096}\sin^2\theta_\ell(z = n_1\delta z, t)$. According to Eq. (26), we need to evaluate $\overline{\Delta\Phi_z}$ (the derivative of ϕ at DW center), which is defined as $\overline{\Delta\Phi_z} = 0.5[\overline{\Delta_1\Phi_{1,z}} + \overline{\Delta_2\Phi_{2,z}}]$, where $\Phi_{\ell,z} = \partial_z\phi_\ell(z)|_{z=0}$ ($\ell = 1, 2$) are the derivative of ϕ_ℓ at DW center, and they are calculated as $\overline{\Delta_\ell\Phi_{\ell,z}} = \frac{1}{200}\sum_{n=1,2,...,200}\Delta_\ell(n\delta t)\partial_z\phi_\ell[z = z_0, n\delta t]$, where $\delta t = 0.1$ ps, $n = 1, 2, ..., 199, 200$.

The symbols in Fig. 6 show $\overline{\Delta\Phi_z}$ (red circles) $\overline{\Delta_1\Phi_{1,z}}$ (blue circles), and $\overline{\Delta_2\Phi_{2,z}}$ (green circles) as functions of current density j for $\beta_\ell = 0.3$ (a), 0.0695 (b), 0.02 (c), and 0 (d). The damping coefficients are fixed as $\alpha_{11} = \alpha_{22} = 0.01$, $\alpha_{12} = \alpha_{21} = 0$. We then fit the $\overline{\Delta\Phi_z}$ (red circles) data under $j > j_W = 4.1 \times 10^{12}\mathrm{A/m^2}$ with a function $c\sqrt{j^2 - j_W^2}$, results are shown by black curves in Fig. 6(a) $\beta_\ell = 0.3$, 6(b) $\beta_\ell = 0.0695$, 6(c) $\beta_\ell = 0.02$, and 6(d) $\beta_\ell = 0$, where the fitting parameter $c = 4.246$ (a), 0.776 (b), 0.139 (c), and -0.124 (d) ($\times 10^{-14}\mathrm{m^2/A}$), respectively.

To see how the fitting parameter c depends on the sublattice nonadiabaticity parameter β_ℓ, we plot c as a function of β_ℓ, as shown by the magenta circles in Fig. 6(e). We find that c depends linearly on β_ℓ and c changes its sign around $\beta_\ell = \alpha_{\ell\ell}$. We thus perform another fitting to the $c - \beta_\ell$ data using a function $c'(\beta_\ell - \alpha_{\ell\ell})$, the fitting parameter is obtained as $c' = 1.46 \times 10^{-13}(\mathrm{m^2/A})$.

We have also compared previous simulations and theory in Ref. [29] with our formula of Eq. (27). For the uniaxial FiM nanowire considered in Ref. [29], $j_W = 0$, our formula of Eq. (27) is $\bar{v} = \frac{\beta P}{\alpha\delta s}\frac{\hbar j}{2e} - c\frac{P}{\alpha\delta s}\frac{\hbar}{2e}j^2$. The coefficients are $\frac{\beta P}{\alpha\delta s}\frac{\hbar}{2e} = -4.35 \times 10^{-9}\beta_1\,\mathrm{m^3/(s\cdot A)}$, $\frac{P}{\alpha\delta s}\frac{\hbar}{2e} = -4.35 \times 10^{-9}\,\mathrm{m^3/(s\cdot A)}$, according to the parameters given in Ref. [29], c is the only fitting parameter. We extract the simulation data (symbols in Fig. 7) and theoretical results (solid curves in Fig. 7) of DW velocity at AMCP from Ref. [29] using an online digitization tool WebPlotDigitizer [64]. Then we fit their simulation data with our formula $\bar{v} = \frac{\beta P}{\alpha\delta s}\frac{\hbar j}{2e} - c\frac{P}{\alpha\delta s}\frac{\hbar}{2e}j^2$, where the fitting parameter $c = -5.109, -3.802, -2.513(\times 10^{-16}\mathrm{m^2/A})$ for $\beta_1 = 0$ (black), 0.0005 (red), 0.001 (blue), respectively. The predictions of our formula are shown by the dashed curves in Fig. 7, it compares much better with the simulation data (symbols) than the previous theoretical formula (solid curves) in Ref. [29].

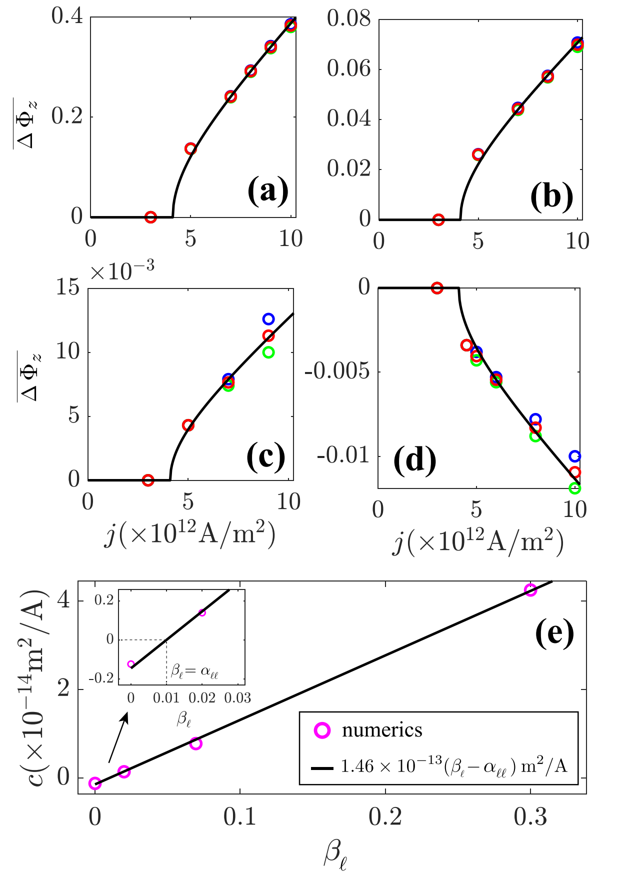

FIG. 6. $\overline{\Delta\Phi_z}$ (red circles), $\overline{\Delta_1\Phi_{1,z}}$ (blue circles), and $\overline{\Delta_2\Phi_{2,z}}$ (green circles) as functions of current density for $\beta_\ell = 0.3$ (a), 0.0695 (b), 0.02 (c), and 0 (d). The damping coefficients are fixed as $\alpha_{11} = \alpha_{22} = 0.01$, $\alpha_{12} = \alpha_{21} = 0$. The black solid curves are fittings results with a function $c\sqrt{j^2 - j_W^2}$. The fitting parameter $c = 4.246$ (a), 0.776 (b), 0.139 (c), and -0.124 (d) ($\times 10^{-14}\mathrm{m^2/A}$). Figure 6(e) plots the fitting parameter c as a function of β_ℓ (magenta circles), the black line in panel (e) is $c = 1.46 \times 10^{-13}(\beta_\ell - \alpha_{\ell\ell})(\mathrm{m^2/A})$, where the coefficient $1.46 \times 10^{-13}(\mathrm{m^2/A})$ is obtained from another fitting. The inset in panel (e) is an enlargement for $\beta_\ell \in [0, 0.03]$, which shows that c changes its sign at $\beta_\ell = \alpha_{\ell\ell} = 0.01$.

IV. DISCUSSIONS AND CONCLUSIONS

We point out that the unphysical negative na-STT found in experiments [20] is based on an incorrect DW velocity formula. This unphysical result does not show up if one use our DW formula near the AMCP which include the DW twisting and high DW precession speed. The DW speed is significantly hindered and not simply proportional to β/α especially in the

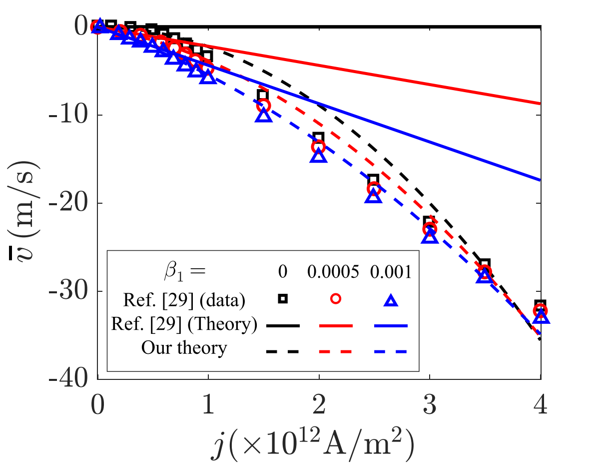

FIG. 7. Comparison between previous results in Ref. [29] and our formula of Eq. (27), for $\beta_1 = 0$ (black), 0.0005 (red), and 0.001 (blue) in a uniaxial wire. The damping coefficients are $\alpha_{11} = \alpha_{22} = 0.002$, $\alpha_{12} = \alpha_{21} = 0$. Symbols (simulation results) and solid lines (theory) are from Ref. [29]. The dashed curves are our Eq. (27), $\bar{v} = \frac{\beta P}{\alpha\delta s}\frac{\hbar j}{2e} - c\frac{P}{\alpha\delta s}\frac{\hbar}{2e}j^2$, with fitting parameter of $c = -5.109, -3.802$, and $-2.513(\times 10^{-16}\mathrm{m^2/A})$ for $\beta_1 = 0$, 0.0005, and 0.001, respectively. The linear coefficient of $\frac{(\beta_1 P_1 + \beta_2 P_2)}{\alpha\delta s}\frac{\hbar}{2e} = -4.35\times 10^{-9}\beta_1\,\mathrm{m^3/(s\cdot A)}$ is from the parameters given in Ref. [29].

case of $\beta > \alpha$. From Eq. (27), the DW mobility should be

$$\mu \equiv \frac{d\bar{v}}{dj} = \frac{\beta P}{\alpha\delta s}\frac{\hbar}{2e} - c\frac{P}{\alpha\delta s}\frac{\hbar}{2e}\frac{2j^2 - j_W^2}{\sqrt{j^2 - j_W^2}}. \tag{28}$$

Existing theories for current-driven DW motion at AMCP have only considered the first term in Eq. (28), which is inconsistent with numerical simulations [29] and experiments in the vicinity of AMCP [20]. The reason is that the second term in Eq. (28) reduces the DW mobility when $j > j_W$, $c > 0$, $P > 0$, leading to a negative β if one only considers the first term in Eq. (28).

In conclusion, we have developed a theory for current-driven DW motion in FiM wires based on generic FiM dynamics and energy-work principle. Our theory provides an insight to the different roles of adiabatic and nonadiabatic torques in current-driven DW motion. Several exact results were obtained. DWs in homogeneous FiM nanowires can resist an a-STT until it reaches a critical value proportional to transverse anisotropy. A static DW cannot exist under an arbitrarily small na-STT. Thus, a DW must move under a na-STT. The total STT does an overall positive work on the DW during its motion, and this positive work compensates the dissipated energy caused by the DW motion. Below the Walker breakdown current, only the na-STT does positive work and the a-STT does no work. Above the Walker breakdown, the DW precesses around the wire axis, the a-STT does either a negative or a positive work, depending on the handedness of DW precession, while the na-STT still does a positive work. Based on the energy-work principle, a DW velocity formula, which agrees with simulations both below and above the Walker breakdown current, is obtained. In the vicinity of AMCP, the DW precession frequency reaches its maximum, accompanied by spin wave emission and large DW structure distortion, which significantly hinders the DW motion. Our theory explains well the observed DW mobility near the AMCP of FiM nanowires and resolves the puzzle of unphysical negative na-STT problem.

ACKNOWLEDGMENTS

This work is supported by the National Key Research and Development Program of China (Grant No. 2020YFA0309600), the National Natural Science Foundation of China (Grant No. 12374122), and Hong Kong RGC (Grants No. 16300522, No. 16300523, and No. 16302321).

APPENDIX A: DERIVATION OF EQS. (18)–(20)

To simplify the three terms on the right-hand side of Eq. (10) in the main text, following assumptions will be used: (1) All spins in the DW almost lie in a plane and $\partial_z\phi \simeq 0$ is a small perturbation. Thus, only leading order or terms not higher than 1 will be kept. (2) The $\theta(z,t)$ profile is well described by the Walker solution. (3) The DW width is approximated by $\Delta(\phi(t)) = \sqrt{\frac{A}{K_z + K_y\sin^2\phi(t)}}$ [40,63]. The validity of these assumptions are verified by micromagnetic simulations in the next Appendix.

Under these assumptions, the dissipation rate is

$$\begin{aligned}\mathcal{P}_\alpha &= -\delta s\frac{\alpha}{1+\alpha^2}\int(\gamma H_\phi + \tau_\theta)^2 + (\gamma H_\theta - \tau_\phi)^2 d^3\boldsymbol{x}\\ &= -S\delta s\frac{2\Delta\alpha}{1+\alpha^2}\left[\left(\frac{K_y\sin 2\phi}{\delta s} + \frac{u}{\Delta}\right)^2 + \left(\frac{\beta u}{\Delta}\right)^2\right],\end{aligned} \tag{A1}$$

where $\tau_\theta = -u\partial_z\theta$, $\tau_\phi = \beta u\partial_z\theta$,

$$\begin{aligned}H_\theta &= \frac{1}{\mu_0(M_1 - M_2)}\left[2A\frac{\partial^2\theta}{\partial z^2} - \frac{\partial f}{\partial\theta} - 2A\sin\theta\cos\theta\left(\frac{\partial\phi}{\partial z}\right)^2\right]\\ &\simeq \frac{1}{\mu_0(M_1 - M_2)}\left(2A\frac{\partial^2\theta}{\partial z^2} - \frac{\partial f}{\partial\theta}\right),\end{aligned} \tag{A2a}$$

$$\begin{aligned}H_\phi &= -\frac{1}{\mu_0(M_1 - M_2)\sin\theta}\frac{\partial f}{\partial\phi}\\ &\quad + \frac{2A}{\mu_0(M_1 - M_2)\sin\theta}\frac{\partial}{\partial z}\left(\sin^2\theta\frac{\partial\phi}{\partial z}\right)\\ &\simeq -\frac{1}{\mu_0(M_1 - M_2)\sin\theta}\frac{\partial f}{\partial\phi} = -\frac{K_y\sin 2\phi\sin\theta}{\mu_0(M_1 - M_2)},\end{aligned} \tag{A2b}$$

and $\gamma = \mu_0(M_1 - M_2)/\delta s$ are used. The final expressions of the effective fields result from $\partial_z\phi = 0$. $H_\theta \simeq 0$ since the Walker solution satisfy $2A\frac{\partial^2\theta}{\partial z^2} - \frac{\partial f}{\partial\theta} = 0$. The integral of $\sin^2\theta$ is the twice of DW width $\int\sin^2\theta dz = 2\Delta$. Multiplying Eq. (A1) by Δ on both sides, the time averaged $\mathcal{P}_\alpha\Delta$ is

$$\begin{aligned}\overline{\mathcal{P}_\alpha\Delta} = &-S\delta s\frac{2\alpha}{1+\alpha^2}\left(\left(\frac{K_y}{\delta s}\right)^2\overline{\Delta^2\sin^2 2\phi} + 2\frac{K_y u}{\delta s}\overline{\Delta\sin 2\phi}\right.\\ &\left. + (1+\beta^2)u^2\right).\end{aligned} \tag{A3}$$

With the following approximations (elaborated in detail at the end of this Appendix),

$$\frac{K_y}{\delta s}\overline{\Delta\sin 2\phi} \simeq \frac{\beta-\alpha}{\alpha}\left(u-\sqrt{u^2-u_W^2}\right), \tag{A4}$$

$$\left(\frac{K_y}{\delta s}\right)^2\overline{\Delta^2\sin^2 2\phi} \simeq \frac{(\beta-\alpha)^2}{\alpha^2}\left(u^2-u\sqrt{u^2-u_W^2}\right), \tag{A5}$$

one has

$$\overline{\mathcal{P}_\alpha\Delta} = 2Su\delta s\left(-\frac{\beta^2 u}{\alpha}+\frac{(\beta^2-\alpha^2)}{\alpha(1+\alpha^2)}\sqrt{u^2-u_W^2}\right). \tag{A6}$$

This is Eq. (18) in the main text.

The power done by a na-STT is

$$\begin{aligned}\mathcal{P}_{\rm na} &= -R_{\rm na} = -\delta s\beta u\int(\partial_t\theta\partial_z\theta+\partial_t\phi\partial_z\phi\sin^2\theta)d^3\boldsymbol{x}\\ &= -S\delta s\beta u\int -v\frac{\sin\theta}{\Delta}\frac{\sin\theta}{\Delta}dz = 2S\delta s\beta u\frac{v}{\Delta}.\end{aligned} \tag{A7}$$

Multiplying Eq. (A7) by Δ on both sides, the time averaged $\mathcal{P}_{\rm na}\Delta$ is

$$\overline{\mathcal{P}_{\rm na}\Delta} = 2S\delta s\beta u\bar{v}. \tag{A8}$$

It explains why DW velocity v is related to $\overline{\mathcal{P}_{\rm na}\Delta}$, instead of $\overline{\mathcal{P}_{\rm na}}$.

The power done by the a-STT is

$$\begin{aligned}\mathcal{P}_{\rm a} &= \delta su\int\boldsymbol{m}\cdot(\partial_t\boldsymbol{m}\times\partial_z\boldsymbol{m})d^3\boldsymbol{x}\\ &= \delta su\int(\partial_t\theta\partial_z\phi-\partial_t\phi\partial_z\theta)\sin\theta d^3\boldsymbol{x}\\ &= -S\delta s\int(\partial_t\phi\sin\theta\partial_z\theta)dz = -2S\delta su\partial_t\phi.\end{aligned} \tag{A9}$$

Substituting Eq. (15) of $\partial_t\phi$ into Eq. (A9) and multiplying both sides by Δ, we can derive Eq. (19),

$$\begin{aligned}\overline{\mathcal{P}_{\rm a}\Delta} &= -2S\delta su\left(\frac{\beta-\alpha}{1+\alpha^2}u-\frac{\alpha\gamma K_y\overline{\Delta\sin 2\phi}}{(1+\alpha^2)\mu_0(M_1-M_2)}\right)\\ &= -2S\delta s\frac{\beta-\alpha}{1+\alpha^2}u\sqrt{u^2-u_W^2}.\end{aligned} \tag{A10}$$

Since $\overline{\Delta dE_{\rm m}/dt}=0$ as explained in main text, one has $\overline{\mathcal{P}_\alpha\Delta}+\overline{\mathcal{P}_{\rm na}\Delta}+\overline{\mathcal{P}_{\rm a}\Delta}=0$. Substituting Eqs. (A6), (A8), and (A10) into the above equation, the equation for $\bar{v}$ is

$$\begin{aligned}&\left(-\frac{\beta^2 u}{\alpha}+\frac{(\beta^2-\alpha^2)}{\alpha(1+\alpha^2)}\sqrt{u^2-u_W^2}\right)+\beta\bar{v}-\frac{\beta-\alpha}{1+\alpha^2}\sqrt{u^2-u_W^2}\\ &\quad = 0,\end{aligned} \tag{A11}$$

which gives Eq. (20) in the main text. The accuracy of Eqs. (A6), (A8), and (A10) have already been discussed in the main text.

To prove Eqs. (A4) and (A5), we start from Eq. (15) which is valid under the approximations mentioned at the beginning of this Appendix. Equation (15) can be expressed in a dimensionless form,

$$\frac{d\phi}{d\tilde{t}} = \frac{\Delta_W}{\Delta}\tilde{j}-\sin 2\phi, \tag{A12}$$

where $\tilde{t}=\frac{\alpha K_y}{(1+\alpha^2)\delta s}t$, $\tilde{j}=\mathrm{sgn}(\beta-\alpha)\frac{j}{j_W}$, $\Delta_W\equiv\max(\Delta\sin 2\phi)=\frac{2}{\sqrt{2\sqrt{1+k}+2+k}}\Delta_0$, with $k=K_y/K_z$, $\Delta_0=\sqrt{A/K_z}$. Δ_W is the maximum of $\frac{\Delta_0\sin 2\phi}{\sqrt{1+k\sin^2\phi}}$ with respect to ϕ. Equation (A12) is difficult to solve in general due to the ϕ-dependence of $\Delta=\frac{\Delta_0}{\sqrt{1+k\sin^2\phi}}$. If one simply assumes $\Delta_W/\Delta=1$, which should not be too bad for small k, then Eq. (A12) becomes

$$\frac{d\phi}{d\tilde{t}} = \tilde{j}-\sin 2\phi. \tag{A13}$$

This equation has static solutions $\phi=0.5(\arcsin\tilde{j})+n\pi$ $(n=0,\pm1,\pm2,\dots)$ which corresponds to the rigid-body DW propagation when $\tilde{j}<1$ $(\phi=-0.5(\arcsin\tilde{j})+0.5n\pi$ are unstable). The solution of this equation for $\tilde{j}>1$ with initial condition $\phi(0)=0$ is

$$\phi(\tilde{t}) = \begin{cases}\arctan\left\{\dfrac{1+\sqrt{\tilde{j}^2-1}\tan\left[\sqrt{\tilde{j}^2-1}\tilde{t}-\arctan\left(\frac{1}{\sqrt{\tilde{j}^2-1}}\right)\right]}{\tilde{j}}\right\} & \tilde{t}\in[0,\tilde{t}_1),\\ \arctan\left\{\dfrac{1+\sqrt{\tilde{j}^2-1}\tan\left[\sqrt{\tilde{j}^2-1}\tilde{t}-\arctan\left(\frac{1}{\sqrt{\tilde{j}^2-1}}\right)\right]}{\tilde{j}}\right\}+n\pi & \tilde{t}\in[\tilde{t}_n,\tilde{t}_{n+1}),\ n=1,2,3,\dots,\end{cases} \tag{A14}$$

where $\tilde{t}_n=\frac{1}{\sqrt{\tilde{j}^2-1}}[\frac{(2n-1)\pi}{2}+\arctan(\frac{1}{\sqrt{\tilde{j}^2-1}})]$. ϕ is continuous and differentiable. The piecewise expression of ϕ is purely because arctangent function is defined in the range of $[-\frac{\pi}{2},\frac{\pi}{2}]$. The solution for $\tilde{j}<-1$ case only differs with Eq. (A14) by an overall minus sign. The period of ϕ-precession is $\tilde{T}=\frac{2\pi}{\sqrt{\tilde{j}^2-1}}$ in the unit of $\frac{(1+\alpha^2)\delta s}{\alpha K_y}$. Equation (A14) is of course not an exact solution of Eq. (A12), but a very nice approximate one. There are at least two reasons for it being a good approximation: (1) Both Eq. (A13) and Eq. (A12) have the same critical current density (j_W). (2) Although ϕ-dependence

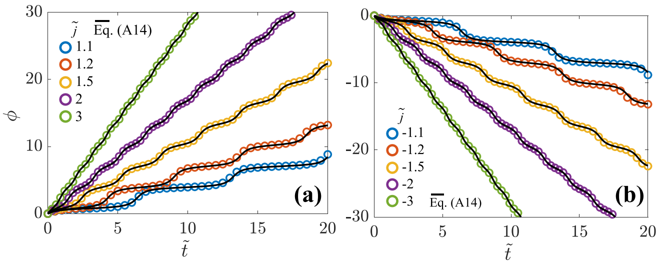

FIG. 8. Azimuthal angle ϕ as a function of t. (a) $\tilde{j} > 0$ and (b) $\tilde{j} < 0$. The symbols are numerical solutions to Eq. (A12) for $|\tilde{j}| = 1.1$ (blue), 1.2 (orange), 1.5 (yellow), 2 (violet), and 3 (green). The black solid curves are Eq. (A14).

of Δ in Eq. (A12) is neglected, the time-dependence of Δ is still kept through its definition. This good approximation can also be checked by the following numerical solutions of Eq. (A12) for $\tilde{j} = 1.1, 1.2, 1.5, 2, 3$ and $\beta > \alpha$, and $\tilde{j} = -1.1, -1.2, -1.5, -2, -3$ and $\beta < \alpha$. Equation (A12) is solved by using a Runge-Kutta solver (ode23) in MATLAB and the results are shown by the dots in Fig. 8. Equation (A14) (black solid curves) compares well with the exact numerical solutions.

With the time-dependent solution of ϕ, $\overline{\Delta \sin 2\phi}$ and $\overline{\Delta^2 \sin^2 2\phi}$ can be computed at least numerically. In the case of $k \ll 1$ such that $\Delta \simeq \Delta_W$, analytical expressions can be found,

$$\begin{aligned}
\overline{\Delta \sin 2\phi} &\simeq \Delta_W \overline{\sin 2\phi} = \frac{\Delta_W}{\tilde{T}} \int_0^{\tilde{T}} \sin 2\phi d\tilde{t} \\
&= \frac{\Delta_W}{\tilde{T}} \int_0^{2\pi} \frac{\sin 2\phi}{\tilde{j} - \sin 2\phi} d\phi \\
&= \frac{\Delta_W}{\tilde{T}} \int_0^{2\pi} -1 + \frac{\tilde{j}}{\tilde{j} - \sin 2\phi} d\phi \\
&= \Delta_W \left(\tilde{j} - \sqrt{\tilde{j}^2 - 1} \right), \qquad \text{(A15)}
\end{aligned}$$

$$\begin{aligned}
\overline{\Delta^2 \sin^2 2\phi} &\simeq \Delta_W^2 \overline{\sin^2 2\phi} = \frac{\Delta_W^2}{\tilde{T}} \int_0^{\tilde{T}} \sin^2 2\phi d\tilde{t} \\
&= \frac{\Delta_W^2}{\tilde{T}} \int_0^{2\pi} \frac{\sin^2 2\phi}{\tilde{j} - \sin 2\phi} d\phi \\
&= \frac{\Delta_W^2}{\tilde{T}} \int_0^{2\pi} -(\tilde{j} + \sin 2\phi) + \frac{\tilde{j}^2}{\tilde{j} - \sin 2\phi} d\phi \\
&= \Delta_W^2 \left(\tilde{j}^2 - \tilde{j}\sqrt{\tilde{j}^2 - 1} \right). \qquad \text{(A16)}
\end{aligned}$$

We have used $\int_0^{2\pi} \frac{1}{\tilde{j} - \sin 2\phi} d\phi = \tilde{T}$ above. Although the expressions of $\overline{\Delta \sin 2\phi}$ and $\overline{\Delta^2 \sin^2 2\phi}$ were obtained from small k approximation, they are surprisingly accurate even for $k = 1, 2$ as shown in Fig. 9. The colored symbols are numerical results of $\phi(\tilde{t})$ of Eq. (A12). The black curves are $\tilde{j} - \sqrt{\tilde{j}^2 - 1}$ (solid line) and $\tilde{j}^2 - \tilde{j}\sqrt{\tilde{j}^2 - 1}$ (dashed line).

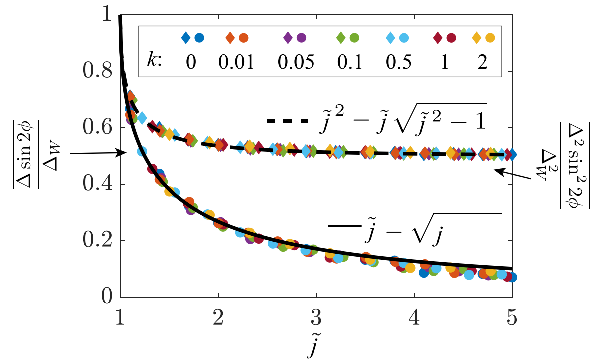

FIG. 9. $\frac{\overline{\Delta \sin 2\phi}}{\Delta_W}$ (circles) and $\frac{\overline{\Delta^2 \sin^2 2\phi}}{\Delta_W^2}$ (diamonds) calculated numerically from Eq. (A12) for $k = 0$ (dark blue), $k = 0.01$ (orange), $k = 0.05$ (violet), $k = 0.1$ (green), $k = 0.5$ (light blue), $k = 1$ (dark red), and $k = 2$ (yellow). The black curves are $\tilde{j} - \sqrt{\tilde{j}^2 - 1}$ (solid line) and $\tilde{j}^2 - \tilde{j}\sqrt{\tilde{j}^2 - 1}$ (dashed line).

$\frac{\overline{(\Delta \sin 2\phi)}}{\Delta_W} \simeq \tilde{j} - \sqrt{\tilde{j}^2 - 1}$ and $\frac{\overline{(\Delta^2 \sin^2 2\phi)}}{\Delta_W^2} \simeq \tilde{j}^2 - \tilde{j}\sqrt{\tilde{j}^2 - 1}$ are exactly Eqs. (A4) and (A5) with $\tilde{j} = \text{sgn}(\beta - \alpha)\frac{u}{u_W}$ and $u_W = \alpha K_y \Delta_W / (\delta s |\beta - \alpha)|)$. More explicitly, $\frac{K_y u}{\delta s} \overline{\Delta \sin 2\phi} = \frac{K_y u \Delta_W}{\delta s} \frac{\overline{(\Delta \sin 2\phi)}}{\Delta_W} = \frac{\beta - \alpha}{\alpha} u(u - \sqrt{u^2 - u_W^2})$, $(\frac{K_y}{\delta s})^2 \overline{\Delta^2 \sin^2 2\phi} = (\frac{K_y \Delta_W}{\delta s})^2 \frac{\overline{(\Delta^2 \sin^2 2\phi)}}{\Delta_W^2} = \frac{(\beta - \alpha)^2}{\alpha^2}(u^2 - u\sqrt{u^2 - u_W^2})$.

APPENDIX B: VERIFICATION OF APPROXIMATIONS IN APPENDIX A

To demonstrate the excellence of approximations used in Appendix A, we carried out MuMax3 simulations of Eq. (2) for a DW motion in a FiM wire of 8 nm × 2 nm × 2048 nm under current densities of $j = 5 \times 10^{12}$ A/m^2 $> j_W = 1.24 \times 10^{12}$ A/m^2 for $\beta = 0.75 > \alpha = 0.1736$, and $j = 8 \times 10^{12}$ A/m^2 $> j_W = 4.1 \times 10^{12}$ A/m^2 for $\beta = 0 < \alpha = 0.1736$, identical to those used in Sec. II B. The mesh size in the simulations is 1 nm × 1 nm × 0.5 nm, thus the top layer is for $\boldsymbol{m}_1$ and the bottom layer is for $\boldsymbol{m}_2$. The x direction consists of eight elements, labeled by $x = 1, \ldots, 8$.

We recorded DW structures $\theta_\ell(x, z, n\delta t)$ and $\phi_\ell(x, z, n\delta t)$ every $\delta t = 0.1$ ps for a duration of 50 ps ($= 1, \ldots 500$), where $\ell = 1, 2$ are for the top and bottom layers, respectively. The average polar and azimuthal angles along the z direction is defined as $\theta(z, n\delta t) = \frac{1}{16} \sum_{x=1,2,\ldots,8} [\theta_1(x, z, \delta t) - \theta_2(x, z, n\delta t)]$ and $\phi(z, n\delta t) = \frac{1}{16} \sum_{x=1,2,\ldots,8} [\phi_1(x, z, \delta t) + \phi_2(x, z, n\delta t) - \pi]$. Figure 10 shows the snapshots of $\tan\phi$ [Figs. 10(a) and 10(b)] and $\cos\theta$ [Figs. 10(c) and 10(d)] for $j = 5 \times 10^{12}$A/m^2 $> j_W = 1.24 \times 10^{12}$A/m^2 and $\beta = 0.75 > \alpha = 0.1736$ [Figs. 10(a) and 10(c)] at $t = 1$ ps (dark blue dots), $t = 5$ ps (orange dots), $t = 9$ ps (yellow dots), $t = 15$ ps (violet dots), and $t = 19$ ps (green dots); and for $j = 8 \times 10^{12}$A/m^2 $> j_W = 4.1 \times 10^{12}$A/m^2 and $\beta = 0 < \alpha = 0.1736$ [Figs. 10(b) and 10(d)] at $t = 1$ ps (dark blue dots), $t = 13$ ps (orange dots), $t = 18$ ps (yellow dots), $t = 23$ ps (violet dots), $t = 37$ ps (green dots), and $t = 41$ ps (light blue dots). The simulation data show small DW plane twisting (z-dependence of ϕ) such that the existence of a DW plane

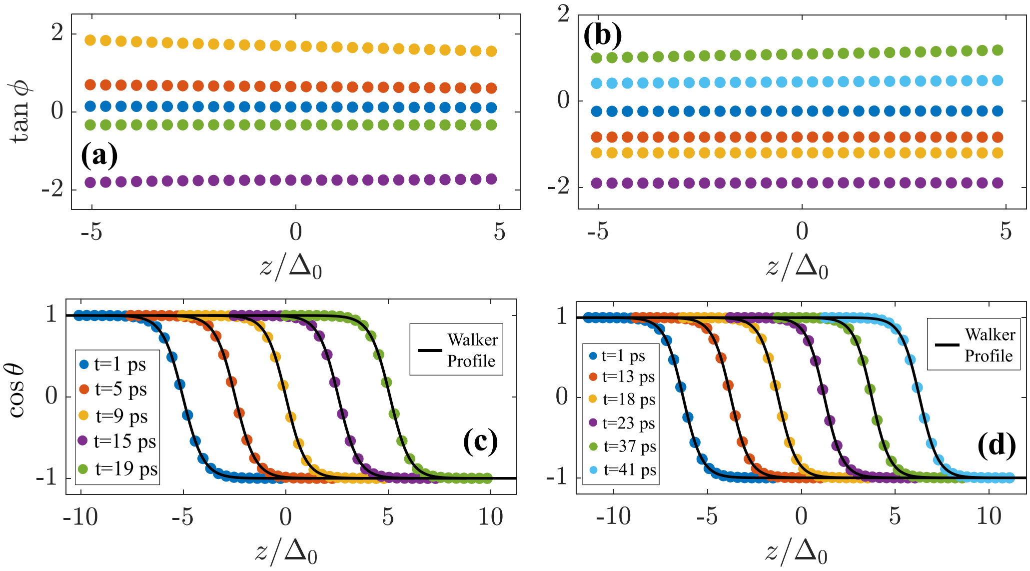

FIG. 10. Snapshots of $\tan\phi$ (a), (b) and $\cos\theta$ (c), (d) as functions of z. Panels (a) and (c) are for $j = 5\times10^{12}\mathrm{A/m^2} > j_W = 1.24\times10^{12}\mathrm{A/m^2}$, $\beta = 0.75 > \alpha = 0.1736$ at $t = 1$ ps (dark blue), $t = 5$ ps (orange), $t = 9$ ps (yellow), $t = 15$ ps (violet), and $t = 19$ ps (green). Panels (b) and (d) are for $j = 8\times10^{12}\mathrm{A/m^2} > j_W = 4.1\times10^{12}\mathrm{A/m^2}$, $\beta = 0 < \alpha = 0.1736$ at $t = 1$ ps (dark blue), $t = 13$ ps (orange), $t = 18$ ps (yellow), $t = 23$ ps (violet), $t = 37$ ps (green), and $t = 41$ ps (light blue). The solid curves in panels (c), (d) are Walker profiles. The DW width obtained from fitting with Walker profiles are $\Delta(t = 1\,\mathrm{ps}) = 3.94$ nm $\Delta(t = 5\,\mathrm{ps}) = 3.86$ nm, $\Delta(t = 9\,\mathrm{ps}) = 3.78$ nm, $\Delta(t = 15\,\mathrm{ps}) = 3.82$ nm, $\Delta(t = 19\,\mathrm{ps}) = 3.94$ nm in panel (c) and $\Delta(t = 1\,\mathrm{ps}) = 3.93$ nm $\Delta(t = 13\,\mathrm{ps}) = 3.87$ nm, $\Delta(t = 18\,\mathrm{ps}) = 3.84$ nm, $\Delta(t = 23\,\mathrm{ps}) = 3.80$ nm, $\Delta(t = 37\,\mathrm{ps}) = 3.80$ nm $\Delta(t = 41\,\mathrm{ps}) = 3.88$ nm in panel (d). Note that the DW centers in panels (c), (d) are shifted for a better view.

is a good assumption. $\cos\theta(z,t)$ can be fitted well by the Walker profile of $\cos\{2\arctan[\exp(\frac{z-z_0}{\Delta})]\}$ [the black curves in Figs. 10(c) and 10(d)], z_0 is the DW center position (where $m_z = 0$). It justifies our assumption of the Walker profile with a time-dependent DW width in Appendix A. Only $\phi(z,t)$ within $z \in [z_0 - 5\Delta_0, z_0 + 5\Delta_0]$ are collected since ϕ outside this range is not well defined.

We have used $\int \sin^2\theta dz = 2\Delta$ to compute $\Delta(t)$, $\Delta(t) = 0.5\delta z\sum_{n_1=1,2,\dots,4096}\sin^2\theta(z = n_1\delta z, t)$. Figures 11(a) and 11(b) are $\Delta(t)$ versus t from simulations (dots), the formula of $\Delta(t) = \sqrt{\frac{A}{K_z+K_y\sin^2\phi(t)}}$ (orange solid curves) with $\phi(t)$ given by Eq. (A12), and Eq. (A14) (yellow dashed curves) for $j = 5\times10^{12}$ A/m$^2 > j_W = 1.24\times10^{12}$ A/m^2 and $\beta = 0.75 > \alpha = 0.1736$ (a), and for $j = 8\times10^{12}$ A/m$^2 > j_W = 4.1\times10^{12}$ A/m^2 and $\beta = 0 < \alpha = 0.1736$ (b). The nice agreement demonstrates that the instantaneous DW width is well approximated by $\Delta(t) = \sqrt{\frac{A}{K_z+K_y\sin^2\phi(t)}}$.

Figures 11(c) and 11(d) are the comparison of the time-dependence of the magnetic energy E_m from the MuMax3 simulations on Eq. (2) (dots) and the magnetic en-

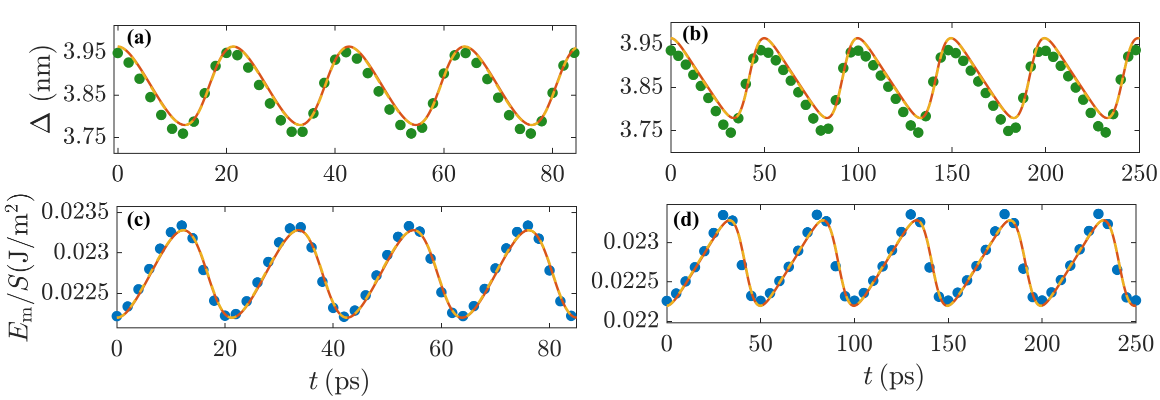

FIG. 11. DW width (green symbols) and DW magentic energy (blue symbols) as functions of time for $j = 5\times10^{12}\mathrm{A/m^2} > j_W = 1.24\times10^{12}\mathrm{A/m^2}$, $\beta = 0.75 > \alpha = 0.1736$ (a), (c), and for $j = 8\times10^{12}\mathrm{A/m^2} > j_W = 4.1\times10^{12}\mathrm{A/m^2}$, $\beta = 0 < \alpha = 0.1736$ (b), (d). Curves are $\Delta(t) = \sqrt{\frac{A}{K_z+K_y\sin^2\phi(t)}}$ (a), (b) and $E_\mathrm{m}/S = 4A/\Delta(t)$. Curves are numerical solution to Eq. (A12) (orange solid curves), and the analytical solution Eq. (A14) (yellow dashed curves).

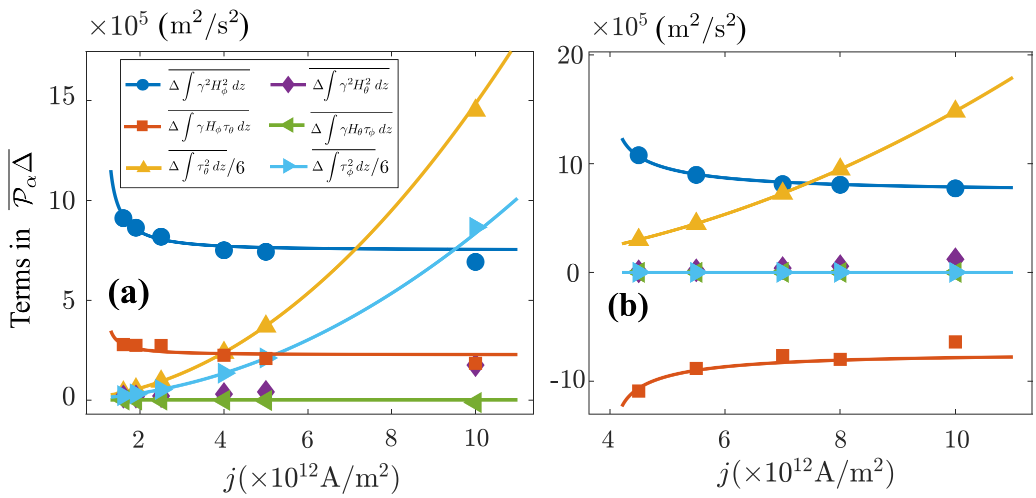

FIG. 12. Current-density dependencies of $\overline{\Delta \int \gamma^2 H_\phi^2 dz}$ (dark blue), $\overline{\Delta \int \gamma H_\phi \tau_\theta dz}$ (orange), $\overline{\Delta \int \tau_\theta^2 dz}/6$ (yellow), $\overline{\Delta \int \gamma^2 H_\theta^2 dz}$ (violet), $\overline{\Delta \int \gamma H_\theta \tau_\phi dz}$ (green), and $\overline{\Delta \int \tau_\phi^2 dz}/6$ (light blue). (a) $\beta = 0.75 > \alpha = 0.1736$. (b) $\beta = 0 < \alpha = 0.1736$. Symbols are simulations and curves are Eqs. (B1)–(B4). For a better visualization, a factor 1/6 is inserted into $\overline{\Delta \int \tau_\theta^2 dz}/6$ and $\overline{\Delta \int \tau_\phi^2 dz}/6$ to make values in the similar ranges.

ergy of $E_{\rm m}(t)/S = \int [A(\partial_z\theta)^2 + (K_z + K_y \sin^2\phi)\sin^2\theta]dz = 4A/\Delta(t) = 4\sqrt{A[K_z + K_y \sin^2\phi(t)]}$ (solid and dashed lines) for $j = 5\times 10^{12}$A/m$^2 > j_W = 1.24\times 10^{12}$A/m^2 for $\beta = 0.75 > \alpha = 0.1736$ (c), and $j = 8\times 10^{12}$A/m$^2 > j_W = 4.1\times 10^{12}$A/m^2 for $\beta = 0 < \alpha = 0.1736$ (d). The calculated energy is based on the assumption of $\partial_z\phi = 0$ [$\phi = \phi(t)$] and $\theta = 2\arctan[\exp(\frac{z-z_0}{\Delta(t)})]$ with $\Delta(t) = \sqrt{\frac{A}{K_z + K_y \sin^2\phi(t)}}$ and $\phi(t)$ of Eq. (A12) [the orange solid curves in Figs. 11(c) and 11(d)] or $\phi(t)$ of Eq. (A14) [the yellow dashed curves in Figs. 11(c) and 11(d)]. The good agreement between simulations results (the symbols) and theoretical prediction (the curves) of DW energy further confirmed the excellent approximations used.

We compared also terms in $\overline{\mathcal{P}_\alpha \Delta}$ directly from MuMax3 simulations and those from our approximations. We verified the terms involved H_θ are indeed close to zero. Figure 12 shows current-density dependencies of $\overline{\Delta \int \gamma^2 H_\phi^2 dz}$ (dark blue), $\overline{\Delta \int \gamma H_\phi \tau_\theta dz}$ (orange), $\overline{\Delta \int \tau_\theta^2 dz}$ (yellow), $\overline{\Delta \int \gamma^2 H_\theta^2 dz}$ (violet), $\overline{\Delta \int \gamma H_\theta \tau_\phi dz}$ (green), and $\overline{\Delta \int \gamma H_\theta \tau_\phi dz}$ (light blue) for $\beta = 0.75 > \alpha = 0.1736$ (a) and $\beta = 0 < \alpha = 0.1736$ (b). The symbols are from the MuMax3 simulations obtained from simulated spin configurations and definitions of effective fields of Eq. (A2a) and (A2b), and definitions of $\tau_\theta = -u\partial_z\theta - \beta u \sin\theta \partial_z\phi$ and $\tau_\phi = -u\sin\theta\partial_z\phi + \beta u \partial_z\theta$. Derivatives of θ and ϕ are numerically obtained from $\partial_z\theta(z,t) = \frac{\theta(z,t)-\theta(z-\delta z,t)}{\delta z}$, $\partial_z\phi(z,t) = \frac{\phi(z,t)-\phi(z-\delta z,t)}{\delta z}$, $\partial_{zz}\theta(z,t) = \frac{\partial_z\theta(z,t)-\partial_z\theta(z-\delta z,t)}{\delta z}$, $\partial_{zz}\phi(z,t) = \frac{\partial_z\phi(z,t)-\partial_z\phi(z-\delta z,t)}{\delta z}$ with $\delta z = 0.5$ nm. Same as before, only data within $z \in [z_0 - 5\Delta_0, z_0 + 5\Delta_0]$ are used for ϕ.

The curves in Fig. 12 are the results from the approximations stated in Appendix A. They are

$$
\begin{aligned}
\overline{\Delta \int \gamma^2 H_\phi^2 dz} &\simeq \left(\frac{K_y}{\delta s}\right)^2 \overline{\Delta \int \sin^2\theta \sin^2 2\phi dz} \\
&= 2\left(\frac{K_y}{\delta s}\right)^2 \overline{\Delta^2 \sin^2 2\phi} \\
&\simeq 2\left(\frac{\beta-\alpha}{\alpha}\right)^2 \left(u^2 - u\sqrt{u^2 - u_W^2}\right) \\
&= 2\left(\frac{\beta-\alpha}{\alpha}\frac{P}{\delta s}\frac{\hbar}{2e}\right)^2 \left(j^2 - j\sqrt{j^2 - j_W^2}\right),
\end{aligned} \tag{B1}
$$

$$
\begin{aligned}
\overline{\Delta \int \gamma H_\phi \tau_\theta dz} &= \frac{K_y}{\delta s} u \overline{\Delta \int \sin\theta \sin 2\phi \frac{\sin\theta}{\Delta} dz} \\
&= 2\frac{K_y}{\delta s} u \overline{\Delta \sin 2\phi} \\
&= 2\left(\frac{\beta-\alpha}{\alpha}\right)\left(u^2 - u\sqrt{u^2 - u_W^2}\right) \\
&= 2\left(\frac{\beta-\alpha}{\alpha}\right)\left(\frac{P}{\delta s}\frac{\hbar}{2e}\right)^2 \left(j^2 - j\sqrt{j^2 - j_W^2}\right)
\end{aligned} \tag{B2}
$$

$$
\overline{\Delta \int \tau_\theta^2 dz} = \overline{\Delta \int u^2 \frac{\sin^2\theta}{\Delta^2} dz} = 2u^2 = 2\left(\frac{P}{\delta s}\frac{\hbar}{2e}\right)^2 j^2, \tag{B3}
$$

$$
\begin{aligned}
&\overline{\Delta \int \gamma^2 H_\theta^2 dz} \simeq 0, \ \overline{\Delta \int \gamma H_\theta \tau_\phi dz} \simeq 0, \\
&\overline{\Delta \int \tau_\phi^2 dz} = \overline{\Delta \int \beta^2 u^2 \frac{\sin^2\theta}{\Delta^2} dz} = 2\beta^2 u^2 \\
&\qquad = 2\beta^2 \left(\frac{P}{\delta s}\frac{\hbar}{2e}\right)^2 j^2.
\end{aligned} \tag{B4}
$$

The simulation results (symbols in Fig. 12) compare well with the approximate analytical expressions Eqs. (B1)–(B4) (solid curves in Fig. 12), which demonstrates the validity of the approximations used. In summary, all the assumptions we made in Appendix A are valid.

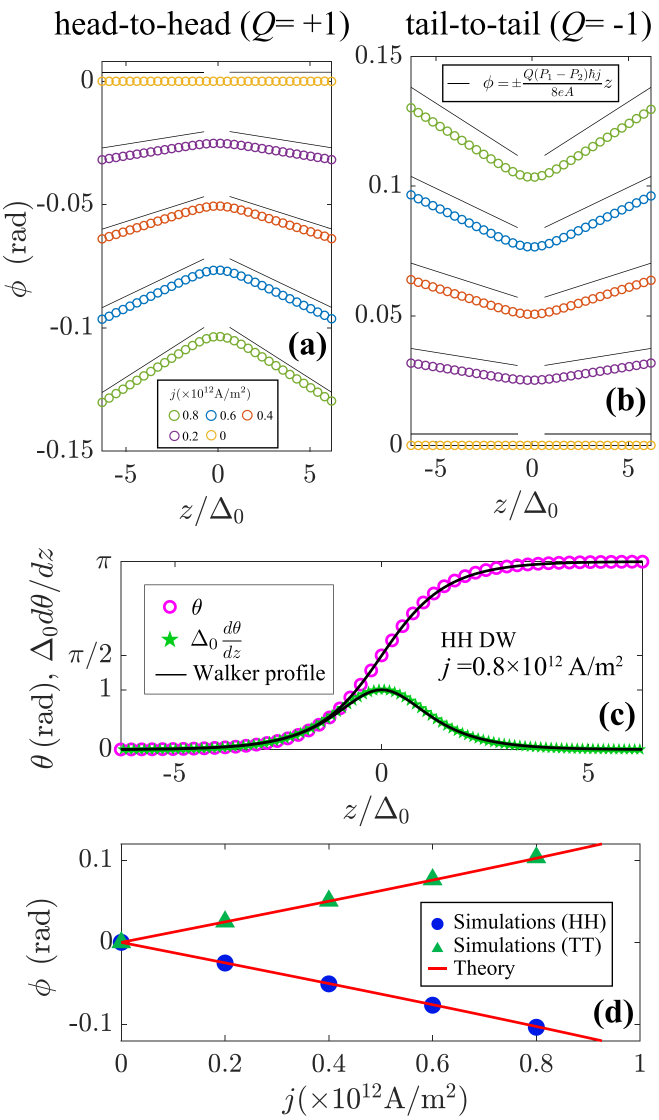

FIG. 13. Distribution of the azimuthal and polar angles of $\boldsymbol{m}$ under different current densities for a HH DW (a) and a TT DW (b) in a cubic-anisotropic wire of $f_\ell = -K_{\ell,z}\cos^2\theta_\ell + K_{\ell,c}(\sin^4\theta_\ell \sin^2\phi_\ell\cos^2\phi_\ell + \sin^2\theta_\ell\cos^2\phi_\ell\cos^2\theta_\ell + \sin^2\theta_\ell\sin^2\phi_\ell\cos^2\theta_\ell)$ with $K_{1,c} = K_{2,c} = 0.1\,\mathrm{MJ/m^3}$. $\Delta_0 = 3.96$ nm, $\alpha_{11} = \alpha_{22} = 0.1$ (we use larger damping coefficients to speed up simulations), $\alpha_{12} = \alpha_{21} = 0$, and other material parameters are specified in Sec. II B. Symbols are simulation results for $j = 0.8$ (green), 0.6 (dark blue), 0.4 (orange), 0.2 (violet), and 0 (yellow) in unit of 10^{12} A/m^2. The slopes of the black solid lines in panels (a, b) are $\pm QP\hbar j/(8eA)$. (c) $\theta(z)$ and $d\theta/dz$ for a HH DW under current $j = 0.8\times10^{12}$ A/m^2. The solid line is the Walker profile. (d) ϕ at the DW center as a function of j. The blue dots and green triangles are for a HH and a TT DW, respectively. The red solid line is Eq. (C1).

APPENDIX C: DW PLANE TWISTING IN CUBIC-ANISOTROPY WIRES

In this Appendix, we demonstrate that a DW plane in cubic-anisotropy wires, $f = -K_z m_z^2 + K_c(m_x^2m_y^2 + m_y^2m_z^2 + m_z^2m_x^2)$, can be twisted by an a-STT. We use MuMax3 [54] (See Sec. II B for details) to solve Eq. (2) in the presence of an a-STT. Starting from a static DW at the center of a nanowireis, ϕ_ℓ of the DW is $0\,(\pi)$ for a HH (TT) DW in the absence of a-STT. An a-STT from various current densities given in Fig. 13 is turned on at $t = 0$. In less than 0.5 ns, the DW becomes static again ($\partial_t\boldsymbol{m}_\ell = \mathbf{0}$), showing the existence of a static DW. The spatial distribution of ϕ for a HH and a TT DW is shown in Figs. 13(a) and 13(b), respectively, in terms of variables of Eq. (3). Spins inside the HH (TT) DW rotate along the wire, either clockwise or counterclockwise. Away from the DW center, the azimuthal angle varies linearly along the wire with a slope of $\pm\frac{QP\hbar j}{8eA}$, indicated by the black solid lines in Figs. 13(a) and 13(b).

For a realistic current density $j = 0.8\times10^{12}\,\mathrm{A/m^2}$ and effective material parameters of $A = 2.2\times10^{-11}$ J/m, $P = 0.4$, $K_z = 1.4\,\mathrm{MJ/m^3}$, $\frac{d\phi}{dz}$ is order of $\frac{P\hbar j}{8eA}\sim 1.2\times10^6\,\mathrm{m^{-1}}$, and $\frac{d\theta}{dz}$ is about $\Delta_0^{-1} = \sqrt{K_z/A}\sim 2.5\times10^8\,\mathrm{m^{-1}}$. Since $\frac{d^2\theta}{dz^2}$, $\frac{1}{2A}\frac{\partial f}{\partial\theta}\sim 10^{16}\,\mathrm{m^{-2}}$, and $(\frac{d\phi}{dz})^2\sin\theta\cos\theta$, $\frac{P\hbar j}{4eA}\frac{d\phi}{dz}\sin\theta\sim 10^{12}\,\mathrm{m^{-2}}$, Eq. (4a) is dominated by the first two terms, 4 orders of magnitude larger than the other two terms. $\theta(z)$ is then well approximated by the Walker profile $\theta(z)\simeq 2\arctan[\exp(Qz/\Delta_0)]$, $d\theta/dz\simeq Q\sin\theta/\Delta_0 = Q\,\mathrm{sech}(z/\Delta_0)/\Delta_0$ as shown in Fig. 13(c) with an excellent agreement between the theory (solid lines) and micromagnetic simulations (symbols) of Eq. (2) for $j = 0.8\times10^{12}\mathrm{A/m^2}$. The good agreements demonstrate that Eq. (4) can well describe the static solutions of Eq. (2). It is worth noting that the spatial variation of ϕ under an a-STT is visible, but very small. Away from the DW center, θ is 0 or π, and ϕ is not well defined and has no significant effect on wire energy and magnetization dynamics.

ϕ at the DW center can also be estimated from energy minimization. Since ϕ does not change much according to analysis above, thus we can express the DW energy $E_\mathrm{m} + E_\mathrm{a}$ as a function of ϕ by integrating over the wire using the Walker profile and constant ϕ. Use $\int_{-\infty}^{+\infty}\sin^2\theta dz = 2\Delta_0$, $\int_{-\infty}^{+\infty}\sin^4\theta dz = \frac{4}{3}\Delta_0$, we have $E_\mathrm{m} + E_\mathrm{a} = S[4\sqrt{AK_z} + \frac{2}{3}\Delta_0K_\mathrm{c} + \frac{1}{3}\Delta_0K_\mathrm{c}\sin^2 2\phi + \frac{QP\hbar j}{e}\phi]$. Minimizing this total energy with respect to ϕ yields the azimuthal angle at the DW center (red solid line),

$$\frac{2}{3}\Delta_0K_\mathrm{c}\sin 4\phi + \frac{QP\hbar j}{e} = 0, \tag{C1}$$

which explains well the data from micromagnetic simulations (dots) as shown in Fig. 13(d).

[1] A. M. Kosevich, B. A. Ivanov, and A. S. Kovalev, Magnetic solitons, Phys. Rep. **194**, 117 (1990).

[2] V. G. Baryakhtar, B. A. Ivanov, A. L. Sukstanskii, and E. Y. Melikhov, Soliton relaxation in magnets, Phys. Rev. B **56**, 619 (1997).

[3] E. G. Galkina and B. A. Ivanov, Dynamic solitons in antiferromagnets, Low Temp. Phys. **44**, 618 (2018).

[4] N. L. Schryer and L. R. Walker, The motion of 180° domain walls in uniform DC magnetic fields, J. Appl. Phys. **45**, 5406 (1974).

[5] Z. Li and S. Zhang, Domain-wall dynamics driven by adiabatic spin-transfer torques, Phys. Rev. B **70**, 024417 (2004).

[6] S. Zhang and Z. Li, Roles of nonequilibrium conduction electrons on the magnetization dynamics of ferromagnets, Phys. Rev. Lett. **93**, 127204 (2004).

[7] A. Thiaville, Y. Nakatani, J. Miltat, and N. Vernier, Domain wall motion by spin-polarized current: A micromagnetic study, J. Appl. Phys. **95**, 7049 (2004).

[8] G. Tatara and H. Kohno, Theory of current-driven domain wall motion: Spin transfer versus momentum transfer, Phys. Rev. Lett. **92**, 086601 (2004).

[9] A. Thiaville, Y. Nakatani, J. Miltat, and Y. Suzuki, Micromagnetic understanding of current-driven domain wall motion in patterned nanowires, Europhys. Lett. **69**, 990 (2005).

[10] Z. Z. Sun, J. Schliemann, P. Yan, and X. R. Wang, Current-induced domain wall motion with adiabatic and nonadiabatic spin torques in magnetic nanowires, Eur. Phys. J. B **79**, 449 (2011)

[11] B. Hu and X. R. Wang, Instability of walker propagating domain wall in magnetic nanowires, Phys. Rev. Lett. **111**, 027205 (2013).

[12] X. S. Wang, P. Yan, Y. H. Shen, G. E. W. Bauer, and X. R. Wang, Domain wall propagation through spin wave emission, Phys. Rev. Lett. **109**, 167209 (2012).

[13] X. S. Wang and X. R. Wang, Thermodynamic theory for thermal-gradient-driven domain-wall motion, Phys. Rev. B **90**, 014414 (2014).

[14] G. Tatara, H. Kohno, and J. Shibata, Microscopic approach to current-driven domain wall dynamics, Phys. Rep. **468**, 213 (2008).

[15] J. Masell and K. Everschor-Sitte, Current-induced dynamics of chiral magnetic structures: Creation, motion, and applications, Top. Appl. Phys. **138**, 147 (2021).

[16] S. S. P. Parkin, M. Hayashi, and L. Thomas, Magnetic domain-wall racetrack memory, Science **320**, 190 (2008).

[17] K.-J. Kim, S. K. Kim, Y. Hirata, S.-H. Oh, T. Tono, D.-H. Kim, T. Okuno, W. S. Ham, S. Kim, G. Go, Y. Tserkovnyak, A. Tsukamoto, T. Moriyama, K.-J. Lee, and T. Ono, Fast domain wall motion in the vicinity of the angular momentum compensation temperature of ferrimagnets, Nat. Mater. **16**, 1187 (2017).

[18] L. Caretta, M. Mann, F. Büttner, K. Ueda, B. Pfau, C. M. Günther, P. Hessing, A. Churikova, C. Klose, M. Schneider, D. Engel, C. Marcus, D. Bono, K. Bagschik, S. Eisebitt, and G. S. D. Beach, Fast current-driven domain walls and small skyrmions in a compensated ferrimagnet, Nat. Nanotechnol. **13**, 1154 (2018).

[19] S. A. Siddiqui, J. Han, J. T. Finley, C. A. Ross, and L. Liu, Current-induced domain wall motion in a compensated ferrimagnet, Phys. Rev. Lett. **121**, 057701 (2018).

[20] T. Okuno, D.-H. Kim, S.-H. Oh, S. K. Kim, Y. Hirata, T. Nishimura, W. S. Ham, Y. Futakawa, H. Yoshikawa, A. Tsukamoto, Y. Tserkovnyak, Y. Shiota, T. Moriyama, K.-J. Kim, K.-J. Lee, and T. Ono, Spin-transfer torques for domain wall motion in antiferromagnetically coupled ferrimagnets, Nat. Electron. **2**, 389 (2019).

[21] E. Haltz, J. Sampaio, S. Krishnia, L. Berges, R. Weil, and A. Mougin, Measurement of the tilt of a moving domain wall shows precession-free dynamics in compensated ferrimagnets, Sci. Rep. **10**, 16292 (2020).

[22] D.-H. Kim, T. Okuno, S. K. Kim, S.-H. Oh, T. Nishimura, Y. Hirata, Y. Futakawa, H. Yoshikawa, A. Tsukamoto, Y. Tserkovnyak, Y. Shiota, T. Moriyama, K.-J. Kim, K.-J. Lee, and T. Ono, Low magnetic damping of ferrimagnetic GdFeCo alloys, Phys. Rev. Lett. **122**, 127203 (2019).

[23] M. V. Logunov, S. S. Safonov, A. S. Fedorov, A. A. Danilova, N. V. Moiseev, A. R. Safin, S. A. Nikitov, and A. Kirilyuk, Domain wall motion across magnetic and spin compensation points in magnetic garnets, Phys. Rev. Appl. **15**, 064024 (2021).

[24] K. Cai, Z. Zhu, J. M. Lee, R. Mishra, L. Ren, S. D. Pollard, P. He, G. Liang, K. L. Teo, and H. Yang, Ultrafast and energy-efficient spin–orbit torque switching in compensated ferrimagnets, Nat. Electron. **3**, 37 (2020).

[25] S. Ghosh, T. Komori, A. Hallal, J. Peña Garcia, T. Gushi, T. Hirose, H. Mitarai, H. Okuno, J. Vogel, M. Chshiev, J.-P. Attané, L. Vila, T. Suemasu, and S. Pizzini, Current-driven domain wall dynamics in ferrimagnetic nickel-doped Mn_4N films: Very large domain wall velocities and reversal of motion direction across the magnetic compensation point, Nano Lett. **21**, 2580 (2021).

[26] J. L. Liu, P. B. He, and M. Q. Cai, Current-driven spiral domain wall in a ferrimagnet near the magnetization compensation point, Phys. Rev. Res. **4**, 023253 (2022).

[27] A. K. Zvezdin, Z. V. Gareeva, and K. A. Zvezdin, Anomalies in the dynamics of ferrimagnets near the angular momentum compensation point, J. Magn. Magn. Mater. **509**, 166876 (2020).

[28] V. V. Yurlov, K. A. Zvezdin, P. N. Skirdkov, and A. K. Zvezdin, Domain wall dynamics of ferrimagnets influenced by spin current near the angular momentum compensation temperature, Phys. Rev. B **103**, 134442 (2021).

[29] D.-H. Kim, D.-H. Kim, K.-J. Kim, K.-W. Moon, S. Yang, K.-J. Lee, and S. K. Kim, The dynamics of a domain wall in ferrimagnets driven by spin-transfer torque, J. Magn. Magn. Mater. **514**, 167237 (2020).

[30] E. Haltz, S. Krishnia, L. Berges, A. Mougin, and J. Sampaio, Domain wall dynamics in antiferromagnetically coupled double-lattice systems, Phys. Rev. B **103**, 014444 (2021).

[31] E. Martínez, V. Raposo, and Ó. Alejos, Novel interpretation of recent experiments on the dynamics of domain walls along ferrimagnetic strips, J. Phys.: Condens. Matter **32**, 465803 (2020).

[32] E. Martínez, V. Raposo, and Ó. Alejos, Current-driven domain wall dynamics in ferrimagnets: Micromagnetic approach and collective coordinates model, J. Magn. Magn. Mater. **491**, 165545 (2019).

[33] B. A. Ivanov, Ultrafast spin dynamics and spintronics for ferrimagnets close to the spin compensation point (Review), Low Temp. Phys. **45**, 935 (2019)

[34] B. A. Ivanov, E. G. Galkina, V. E. Kireev, N. E. Kulagin, R. V. Ovcharov, and R. S. Khymyn, Nonstationary forced motion of domain walls in ferrimagnets near the spin compensation point, Low Temp. Phys. **46**, 841 (2020).

[35] E. G. Galkina, N. E. Kulagin, and B. A. Ivanov, Dynamics of Dzyaloshinskii domain walls for ferrimagnets with compensation of angular momentum, Ann. Phys. (NY) **447**, 169080 (2022).

[36] M. Jin, I.-S. Hong, D.-H. Kim, K.-J. Lee, and S. K. Kim, Domain-wall motion driven by a rotating field in a ferrimagnet, Phys. Rev. B **104**, 184431 (2021).

[37] S.-H. Oh, S. K. Kim, J. Xiao, and K.-J. Lee, Bidirectional spin-wave-driven domain wall motion in ferrimagnets, Phys. Rev. B **100**, 174403 (2019).

[38] A. Donges, N. Grimm, F. Jakobs, S. Selzer, U. Ritzmann, U. Atxitia, and U. Nowak, Unveiling domain wall dynamics of ferrimagnets in thermal magnon currents: Competition of angular momentum transfer and entropic torque, Phys. Rev. Res. **2**, 013293 (2020).

[39] W. H. Li, Z. Jin, D. L. Wen, X. M. Zhang, M. H. Qin, and J. M. Liu, Ultrafast domain wall motion in ferrimagnets induced by magnetic anisotropy gradient, Phys. Rev. B **101**, 024414 (2020).

[40] K. Y. Jing, X. Gong, and X. R. Wang, Field-driven domain wall motion in ferrimagnetic nanowires, Phys. Rev. B **106**, 174429 (2022).

[41] S. K. Kim, G. S. D. Beach, K.-J. Lee, T. Ono, T. Rasing, and H. Yang, Ferrimagnetic spintronics, Nat. Mater. **21**, 24 (2022).

[42] J. Slonczewski, Current-driven excitation of magnetic multilayers, J. Magn. Magn. Mater. **159**, L1 (1996).

[43] X. R. Wang, P. Yan, J. Lu, and C. He, Magnetic field driven domain-wall propagation in magnetic nanowires, Ann. Phys. (NY) **324**, 1815 (2009).

[44] X. R. Wang, P. Yan, and J. Lu, High-field domain wall propagation velocity in magnetic nanowires, Europhys. Lett. **86**, 67001 (2009).

[45] I. M. Miron, T. Moore, H. Szambolics, L. D. B.-Prejbeanu, S. Auffret, B. Rodmacq, S. Pizzini, J. Vogel, M. Bonfim, A. Schuhl, and G. Gaudin, Fast current-induced domain-wall motion controlled by the Rashba effect, Nat. Mater. **10**, 419 (2011).

[46] T. Ono, H. Miyajima, K. Shigeto, K. Mibu, N. Hosoito, and T. Shinjo, Propagation of a magnetic domain wall in a submicrometer magnetic wire, Science **284**, 468 (1999).

[47] G. S. D. Beach, C. Nistor, C. Knutson, M. Tsoi, and J. L. Erskine, Dynamics of field-driven domain-wall propagation in ferromagnetic nanowires, Nat. Mater. **4**, 741 (2005).

[48] A. Yamaguchi, T. Ono, S. Nasu, K. Miyake, K. Mibu, and T. Shinjo, Real-space observation of current-driven domain wall motion in submicron magnetic wires [Phys. Rev. Lett. 92, 077205 (2004)], Phys. Rev. Lett. **92**, 077205 (2004); Erratum: A. Yamaguchi, T. Ono, S. Nasu, K. Miyake, K. Mibu, and T. Shinjo, Real-space observation of current-driven domain wall motion in submicron magnetic wires, **96**, 179904(E) (2006).

[49] H. Y. Yuan, Q. Liu, K. Xia, Z. Yuan, and X. R. Wang, Proper dissipative torques in antiferromagnetic dynamics, Europhys. Lett. **126**, 67006 (2019).

[50] A. Kamra, R. E. Troncoso, W. Belzig, and A. Brataas, Gilbert damping phenomenology for two-sublattice magnets, Phys. Rev. B **98**, 184402 (2018).

[51] R. K. Wangsness, Sublattice effects in magnetic resonance, Phys. Rev. **91**, 1085 (1953).

[52] M. Binder, A. Weber, O. Mosendz, G. Woltersdorf, M. Izquierdo, I. Neudecker, J. R. Dahn, T. D. Hatchard, J.-U. Thiele, C. H. Back, and M. R. Scheinfein, Magnetization dynamics of the ferrimagnet CoGd near the compensation of magnetization and angular momentum, Phys. Rev. B **74**, 134404 (2006).

[53] C. D. Stanciu, A. V. Kimel, F. Hansteen, A. Tsukamoto, A. Itoh, A. Kiriliyuk, and T. Rasing, Ultrafast spin dynamics across compensation points in ferrimagnetic GdFeCo: The role of angular momentum compensation, Phys. Rev. B **73**, 220402(R) (2006).

[54] A. Vansteenkiste, J. Leliaert, M. Dvornik, M. Helsen, F. G. Sanchez, and B. V. Waeyenberge, The design and verification of MuMax3, AIP Adv. **4**, 107133 (2014).

[55] I. Radu, K. Vahaplar, C. Stamm, T. Kachel, N. Pontius, H. A. Dürr, T. A. Ostler, J. Barker, R. F. L. Evans, R. W. Chantrell, A. Tsukamoto, A. Itoh, A. Kirilyuk, Th. Rasing, and A. V. Kimel, Transient ferromagnetic-like state mediating ultrafast reversal of antiferromagnetically coupled spins, Nature (London) **472**, 205 (2011).

[56] C. E. Patrick, S. Kumar, G. Balakrishnan, R. S. Edwards, M. R. Lees, L. Petit, and J. B. Staunton, Calculating the magnetic anisotropy of rare-earth-transition-metal ferrimagnets, Phys. Rev. Lett. **120**, 097202 (2018).

[57] M. Ding and S. J. Poon, Tunable perpendicular magnetic anisotropy in GdFeCo amorphous films, J. Magn. Magn. Mater. **339**, 51 (2013).

[58] H. Damas, A. Anadon, D. C. Berrocal, J. A. Saenz, J. Bello, A. A. Córdova, S. Migot, J. Ghanbaja, O. Copie, M. Hehn, V. Cros, S. P. Watelot, and J. C. R. Sánchez, Ferrimagnet GdFeCo characterization for spin-orbitronics: Large field-like and damping-like torques, Phys. Status Solidi RRL **16**, 2200035 (2022).

[59] L. Shen and K. Shen, Skyrmion-based chaotic oscillator driven by a constant current, Phys. Rev. B **109**, 014422 (2024).

[60] L. Liensberger, A. Kamra, H. Maier-Flaig, S. Geprägs, A. Erb, S. T. B. Goennenwein, R. Gross, W. Belzig, H. Huebl, and M. Weiler, Exchange-enhanced ultrastrong magnon-magnon coupling in a compensated ferrimagnet, Phys. Rev. Lett. **123**, 117204 (2019).

[61] See Supplemental Material at http://link.aps.org/supplemental/10.1103/PhysRevB.110.054414 for six videos showing strong spin wave emission around the AMCP when the applied current is above the Walker breakdown current (videos 1–4), in comparison with no significant spin wave emissions away from AMCP (videos 5 and 6).

[62] O. Tchernyshyov, Unified theory of spin and charge in a ferromagnet, J. Phys.: Condens. Matter **35**, 014001 (2023).

[63] *Spin Dynamics in Confined Magnetic Structures III*, edited by B. Hillebrands and A. Thiaville, Topics in Applied Physics (Springer, Berlin, Heidelberg, 2006).

[64] A. Rohatgi, WebPlotDigitizer: Version 4.6 (2022), https://automeris.io/.